

BIPP: An efficient HPC implementation of the Bluebild algorithm for radio astronomy

Emma Tolley^{a,b}, Simon Frasca^c, Etienne Orliac^b, Shreyam Krishna^a, Michele Bianco^a, Sepand Kashani^a, Paul Hurley^d, Matthieu Simeoni^a, Jean-Paul Kneib^a

^aInstitute of Physics, Laboratory of Astrophysics, École Polytechnique Fédérale de Lausanne (EPFL), Observatoire de Sauverny, Versoix, 1290, Switzerland

^bSCITAS, École Polytechnique Fédérale de Lausanne (EPFL), Lausanne, 1015, Switzerland

^cSwiss National Supercomputing Centre (CSCS), Switzerland

^dWestern Sydney University, Penrith, Australia

Abstract

The Bluebild algorithm is a new technique for image synthesis in radio astronomy which decomposes the sky into distinct energy levels using functional principal component analysis. These levels can be linearly combined to construct a least-squares estimate of the radio sky, i.e. minimizing the residuals between measured and predicted visibilities. This approach is particularly useful for deconvolution-free imaging or for scientific applications that need to filter specific energy levels. We present an HPC implementation of the Bluebild algorithm for radio-interferometric imaging: Bluebild Imaging++ (BIPP). The library features interfaces to C++, C and Python and is designed with seamless GPU acceleration in mind. We evaluate the accuracy and performance of BIPP on simulated observations of the upcoming Square Kilometer Array Observatory and real data from the Low-Frequency Array (LOFAR) telescope. We find that BIPP offers accurate wide-field imaging and has competitive execution time with respect to the interferometric imaging libraries CASA and WSClean for images with $\leq 10^6$ pixels. Furthermore, due to the energy level decomposition, images produced with BIPP can reveal information about faint and diffuse structures before any cleaning iterations. BIPP does not perform any regularization, but we suggest methods to integrate the output of BIPP with CLEAN. The source code of BIPP is publicly released.

Keywords: instrumentation: interferometers – methods: observational – techniques: interferometric – radio continuum: general

1. Introduction

Radio astronomers are engaged in ambitious new projects to detect faster, fainter, and more distant astrophysical phenomena. The flagship project is the Square Kilometer Array Observatory (SKAO)¹ (Dewdney et al., 2009), and is considered to be one of the major “Big Data” challenges of the next decade. According to the SKA estimates (Broekema et al., 2015), the SKAO Science Data Processor (SDP) workflow will need to be able to deal with a data flow rate of around 1 TB/s at full capacity and will require a supercomputer of around 100 Pflops to calibrate and image the data.

A major task of the SDP workflow will be *image synthesis*: reconstructing an estimate of the radio sky I using finite measurements of visibility space $V \in \mathbb{C}^{L \times L}$. Image synthesis involves Fourier-transforming the calibrated visibilities into the “dirty” image (also known as the backprojected image). After imaging, deconvolution corrects the resulting images for the incomplete sampling of the Fourier plane. This step is typically performed using the CLEAN family of algorithms (Högbom, 1974), which use a point-source model and iterative deconvolution to extract a final “clean” image of the sky.

Imaging is one of the most computationally demanding steps in the data processing pipeline, requiring significant memory and computing power. This complexity arises from operations

like gridding, the convolutional resampling of observed data onto a regular grid, and fast Fourier transforms (FFT; Frigo and Johnson (1997, 2005)) to transition between visibility and image space. The computational demands increase for observations of large fields of view (FoVs) where curvature effects cannot be neglected. Various algorithms have been developed to leverage the log-linear complexity of the 2D FFT, such as the w-stacking algorithm (Offringa et al., 2014) used by WSClean, the w-projection technique (Cornwell et al., 2008) used by CASA (The CASA Team, 2022), and faceting (Cornwell and Perley, 1992) used by DDFacet (Tasse et al., 2018). Many other techniques have been explored for the different steps of image synthesis, for example using 3D NUFFT (Kashani et al., 2023), optimization methods (Wilber et al., 2023), or artificial intelligence (Schmidt et al., 2022).

The Bluebild algorithm (Kashani, 2017) offers a new approach to image synthesis. Bluebild is a method for reconstructing a least-squares consistent image of the sky based on the theory of sampling and interpolation operators (Vetterli et al., 2014). Image formation is formulated as a continuous inverse problem, and a key innovation of Bluebild is to use functional principal component analysis (fPCA) decomposition to simplify calculations of the sky image. Bluebild addresses the gridding, fast Fourier transform, and w-correction steps of imaging.

Image synthesis algorithms for next-generation radio interferometers must be able to handle the data sizes of the fu-

¹<https://www.skao.int/>

ture SKAO. Their implementations must be parallelizable, scalable, and portable. In this paper, we provide an overview of the Bluebird algorithm and present our HPC implementation BIPP: Bluebird Imaging++. We show extensive validation results, comparing the output of BIPP to WSClean (Offringa et al., 2014; Offringa and Smirnov, 2017) and CASA (The CASA Team, 2022), and evaluate the performance of the BIPP library. Finally, we explore the effect of the fPCA decomposition on image reconstruction and discuss scientific applications and future directions.

2. The Bluebird Algorithm

2.1. Astronomical Measurement Equations

Electric fields emitted by astrophysical sources can be described by a continuous complex distribution $E(\vec{r}, f, t)$, where \vec{r} is a (unit) direction vector denoting the sky coordinate. A radio antenna indexed by p located at position $\vec{x}_p \in \mathbb{R}^3$ will measure the phased sum of these electric fields over the entire sky as a voltage $v_p \in \mathbb{C}$ given by (Thyagarajan et al., 2017):

$$v_p(f, t) = \int E(\vec{r}, f, t) g_p(\vec{r}, f, t) \phi_p(\vec{r}, f) d\Omega + n_p(f, t), \quad (1)$$

where $g_p(\vec{r}, f, t)$ is the directional antenna voltage response at a given frequency and time, $\phi_p(\vec{r}, f) \equiv \exp\left\{-\frac{2\pi i f}{c} \langle \vec{x}_p, \vec{r} \rangle\right\}$ is the steering vector of the instrument (Simeoni and Hurley, 2019), also known as the phase delay term, and $n_p(f, t)$ is uncorrelated additive receiver noise. If we discretize \vec{r} into N_{sky} discrete coordinates indexed by j , we can write the discrete form of Eq. 1:

$$v_p(f, t) = \sum_j^{N_{\text{sky}}} E_j(f, t) g_{pj}(f, t) e^{-\frac{2\pi i f}{c} \langle \vec{x}_p, \vec{r}_j \rangle} + n_p(f, t). \quad (2)$$

By introducing introduce a time- and frequency-dependent matrix known as the sampling operator $\Psi^* \in \mathbb{C}^{N_A \times N_{\text{sky}}}$ with elements defined as

$$\Psi_{pj}^* = g_{pj} e^{\frac{2\pi i f}{c} \langle \vec{x}_p, \vec{r}_j \rangle}, \quad (3)$$

we can write Eq. 2 concisely in matrix notation:

$$\vec{v} = \Psi^* \vec{E} + \vec{\eta}, \quad (4)$$

where $\vec{v} \in \mathbb{C}^{N_A}$ is the vector of voltages recorded over all N_A antennas, $\vec{E} \in \mathbb{C}^{N_{\text{sky}}}$ is the vector of electric fields across the discretized sky coordinates, and $\vec{\eta} \in \mathbb{C}^{N_A}$ is the vector of noise terms across all antennas. For conciseness we have dropped the explicit dependence on frequency and time, but note that Ψ , $\vec{\eta}$, \vec{E} , and \vec{v} are all frequency- and time-dependent.

Interferometers measure visibilities, the voltage correlation between two antennas p and q (Hamaker et al., 1996; Rau et al., 2009; Smirnov, 2011; van der Veen and Wijnholds, 2013). The voltage correlation matrix, also known as the visibility matrix, is given by:

$$V \equiv \mathbb{E}[\vec{v}\vec{v}^*] = \Psi^* B \Psi + \sigma^2 \mathbb{I}, \quad (5)$$

where \mathbb{I} is the identity matrix, the noise correlation matrix is $\sigma^2 \mathbb{I} = \mathbb{E}[\vec{\eta}\vec{\eta}^*]$, and B is the correlation matrix of the discretized

electric field emission \vec{E} : $B = \mathbb{E}[\vec{E}\vec{E}^*]$. Because signals coming from different directions in the sky are uncorrelated (Taylor et al., 1999), B is a diagonal matrix with diagonal elements given by $B_{jj} = |E_j|^2$. For concise notation in later derivations, we define the sky brightness vector \vec{I} as the diagonal of B :

$$I_j \equiv B_{jj} = |E_j|^2. \quad (6)$$

2.2. The Inverse Problem

Image synthesis in radio astronomy seeks to reconstruct an estimate of B from discrete measurements of V :

$$V = \Psi^* B \Psi + \sigma^2 \mathbb{I}. \quad (7)$$

We can try to construct an estimate of B called \tilde{B} which satisfies the *least-squares* problem, i.e. minimizes the following expression:

$$\|\Psi^* \tilde{B} \Psi - V\|^2, \quad (8)$$

The solution to this is well known and takes the form:

$$\tilde{B} = \Psi G_{\Psi}^{-1} V G_{\Psi}^{-1} \Psi^*, \quad (9)$$

where $G_{\Psi} \in \mathbb{C}^{N_A \times N_A}$ is the *Gram matrix* of the instrument defined as $G_{\Psi} \equiv \Psi^* \Psi$:

$$(G_{\Psi})_{pq} = \sum_j^{N_{\text{sky}}} \Psi_{pj}^* \Psi_{jq} = \sum_j^{N_{\text{sky}}} g_{pj} g_{qj}^* e^{2\pi i f \langle \vec{b}_{pq}, \vec{r}_j \rangle} \quad (10)$$

where \vec{b}_{pq} is the baseline vector between antennas p and q : $\vec{b}_{pq} \equiv \frac{f}{c} (\vec{x}_p - \vec{x}_q)$. In the case of calibrated omnidirectional antennas we can write $g_p(\vec{r}) = 1$, and the Gram matrix can be shown to have the following analytical closed form (at the continuous level) (Kashani, 2017):

$$(G_{\Psi})_{pq} = \text{sinc}\left(2 \left\| \vec{b}_{pq} \right\| \right). \quad (11)$$

Unfortunately, the Gram matrix can be ill-conditioned (Taylor, 1978), hence evaluating its inverse in Eq. 9 is prone to error.

2.3. Functional Principal Component Analysis

The Bluebird algorithm (Kashani, 2017) calculates \tilde{B} and thus \vec{I} from Equation 9 by directly finding a decomposition of \tilde{B} in a compact orthogonal basis, namely

$$\tilde{B} = \sum_a \lambda_a \epsilon_a \epsilon_a^H = \sum_a \lambda_a \Psi \alpha_a \alpha_a^H \Psi^*, \quad (12)$$

where $\{(\lambda_a, \epsilon_a \equiv \Psi \alpha_a)\} \in \mathbb{R} \times \mathbb{C}^{N_{\text{sky}}}$ are eigenpairs of \tilde{B} . The relation $\epsilon_a = \Psi \alpha_a$, where $\alpha_a \in \mathbb{C}^{N_A}$ follows since $\epsilon_a \subset \text{span}(\Psi)$. The parameters $\{(\lambda_a, \alpha_a)\}$ can easily be inferred starting from the eigenvalue property:

$$\tilde{B} \epsilon_a = \lambda_a \epsilon_a.$$

Combining the above with the expression for \tilde{B} in Equation 9 and using $\epsilon_a \equiv \Psi \alpha_a$ we obtain:

$$(\Psi G_{\Psi}^{-1} V G_{\Psi}^{-1} \Psi^*) \Psi \alpha_a = \lambda_a \Psi \alpha_a$$

Using $G_\Psi = \Psi^* \Psi$, this reduces to:

$$V\alpha_a = \lambda_a G_\Psi \alpha_a. \quad (13)$$

Thus the parameters $\{(\lambda_a, \alpha_a)\}$ are obtained by solving the generalized eigenvalue problem $V\alpha_a = \lambda_a G_\Psi \alpha_a$. This allows us to calculate the least-squares solution without inverting G_Ψ , giving:

$$\tilde{I} = \sum_a \lambda_a |\epsilon_a|^2 = \sum_a \lambda_a |\Psi \alpha_a|^2. \quad (14)$$

Recall that V and Ψ are time and frequency dependent, so \tilde{I} is an estimate of the instantaneous narrow-band sky intensity. Thus the eigenvalue decomposition in Eq. 13 must be repeated for each timestep t and frequency band f . It can be shown that the time-integrated LSQ image $\sum_t \tilde{I}(t)$ will also be a LSQ solution if the corresponding Gram matrix for the integrated operator is block-diagonal, which is true if $\|\vec{x}_p(t) - \vec{x}_q(t + \Delta t)\| \gg \lambda$ for all p and q , with wavelength $\lambda = f/c$ and integration time Δt . For $\lambda = 6\text{m}$ and an observing latitude of 30° this assumption holds for $\Delta t > 0.02\text{s}$.

2.4. Standard Image Synthesis

After obtaining our eigenpairs (λ_a, α_a) , we can reconstruct ϵ_a by directly applying the complex conjugate of the sampling operator Ψ :

$$\epsilon_{aj} = \sum_p \Psi_{jp} \alpha_{ap} = \sum_p g_{pj}^* e^{-\frac{2\pi i f}{c} \langle \vec{x}_p, \vec{r}_j \rangle} \alpha_{ap}. \quad (15)$$

Directly calculating this result via matrix multiplication is called *Standard Synthesis*. Because \vec{b}_p is comprised of the instantaneous antenna positions, Ψ is a time- and frequency-dependent operator, and Eq. 15 must be evaluated at each timestep.

2.5. NUFFT Image Synthesis

We can improve Standard Synthesis by leveraging algorithms for non-uniform FFT (NUFFT; Lee and Greengard, 2005) of type-3, which maps from a non-uniform input domain to a non-uniform output domain (Bagchi and Mitra, 1999). The expression for our least-squares reconstructed sky can be expanded as

$$\tilde{I} = \sum_a \lambda_a |\epsilon_a|^2 = \Psi V' \Psi^*, \quad (16)$$

where V' are the Gram-corrected visibilities

$$V' = A \Lambda A^H, \quad (17)$$

where the columns of matrix $A \in \mathbb{C}^{N_A \times N_A}$ are the ordered eigenvectors α_a and Λ is a diagonal matrix with diagonal elements as the ordered eigenvalues λ_a . Writing out Ψ explicitly and assuming calibrated gains $g_p(\vec{r}) = 1$, Equation 16 can be expressed as a discrete Fourier transform:

$$\tilde{I}_j = \sum_p \sum_q V'_{pq} e^{-2\pi i \langle \vec{b}_{pq}, \vec{r}_j \rangle}. \quad (18)$$

We can consolidate the sum over separate baselines by choosing an appropriate index n for the baselines created by antenna pairs p and q :

$$\tilde{I}_j = \sum_n^{N_A \times N_A} V'_n e^{-2\pi i \langle \vec{b}_n, \vec{r}_j \rangle}, \quad (19)$$

We have N_A^2 samples of the visibilities V'_n at coordinates \vec{b}_n in the uvw plane, and map to N_{sky} coordinates in the sky. This can be evaluated with a type-3 NUFFT (Kashani et al., 2023), which performs the familiar gridding/degridding operations as defined in Section 3.4. We call this alternative imaging strategy *NUFFT Synthesis*.

2.6. Energy Levels & Partitioning

A key aspect of the Bluebird algorithm is decomposing the sky into distinct eigenvalue-eigenvector pairs $\{(\lambda_a, \alpha_a)\}$ as shown in Equation 14. These levels can be manipulated via truncation, partitioning, or filtering to create different output images.

Truncation: not every eigenvector α_a needs to be used for constructing the LSQ sky intensity estimate \tilde{I} . As the eigenvectors with the smallest eigenvalues often correspond to noise, BIPP includes an option only to construct images using $N_{\text{eig}} \leq N_A$ leading eigenvectors. N_{eig} can be set to the total number of eigenvalues N_A , a custom value defined by the user, or estimated from a given observation by determining the minimum number of leading eigenvectors that account for a user-defined percentage of the total energy. Discarding the smallest-energy levels allows for efficient suppression of noise in the reconstructed image. Alternatively, the largest eigenvectors can be discarded to remove the brightest point sources.

Partitioning: for the imaging process, the $\{(\lambda_a, \alpha_a)\}$ pairs can optionally be partitioned or grouped into $N_L \leq N_A$ energy levels. A level consists of n eigenpairs i_0 through i_n . In Standard Synthesis, this is defined by:

$$\tilde{I}_{i_0, i_n} = \sum_{a=i_0}^{a=i_n} \lambda_a |\epsilon_a|^2 \quad (20)$$

In NUFFT synthesis the levels are defined at the visibility level, minimizing the numbers of calls to the type-3 NUFFT:

$$\tilde{I}_{i_0, i_n} = \Psi V'_{i_0, i_n} \Psi^*. \quad (21)$$

V'_{i_0, i_n} is constructed by setting eigenvalues which fall outside the interval to zero. Level partitions can be automatically determined using k -means clustering on the eigenvalues $\{\lambda_a\}$, or defined as intervals by the user. Combining the N_A eigenvectors into a smaller number of levels reduces the total number of calls to Standard Synthesis or NUFFT Synthesis during imaging. Examples of partitioned images output by BIPP are shown in Section 6.

Finally, eigenvalues and eigenvectors can be using user-defined **filters** to create different images with different weights. One possible filter is *Least-Squares (LSQ)*, which combines the eigenvectors ϵ_a after re-weighting them at their true scale λ_a as in Equation 14, thus producing an image minimizing the

least-squares optimization problem. Alternatively, a *Standardized* image can be constructed by performing a uniform sum across eigenvectors $\{\epsilon_a\}$, effectively normalizing the flux across all eigenimages.

2.7. Beamforming

For certain telescopes, the N_A antenna voltages \vec{v} are not available directly but are instead beamformed together into K beams using a weighting matrix $W \in \mathbb{C}^{N_A \times K}$ (Açal et al., 2015). The beamformed voltages $\vec{v}^W \in \mathbb{C}^K$ are then given by:

$$\vec{v}_k^W = W \vec{v}. \quad (22)$$

We can define a modified sampling operator, which includes beamforming $\Phi^* = W^H \Psi^*$. The beamformed visibilities $V^W \in \mathbb{C}^{K \times K}$ are thus given by:

$$V^W = \Phi^* B \Phi = W^H \Psi^* B \Psi W, \quad (23)$$

and with this new sampling operator the Gram matrix $G_\Psi^W \in \mathbb{C}^{K \times K}$ becomes:

$$G_\Psi^W = \Phi^* \Phi = W^H \Psi^* \Psi W. \quad (24)$$

Beamforming can easily be accommodated in Standard Synthesis and NUFFT Synthesis with the redefined sampling operator Φ^* .

2.8. Comparison with CLEAN

The CLEAN algorithm (Högbom, 1974) and its variants (Clark, 1980; Cornwell, 2008) use an iterative method to construct an estimate of B (Van der Tol et al., 2018). *Back-projection* is used to construct an initial estimate \hat{B} :

$$\hat{B} = \Psi V \Psi^*. \quad (25)$$

We can write out \hat{B} explicitly:

$$\hat{B}_{jj} = \hat{I}_j = \sum_p \sum_q^{N_A} \Psi_{pj} V_{pq} \Psi_{qj}^* = \sum_s^{N_A \times N_A} V_s e^{-2\pi i \langle \vec{b}_s, \vec{r}_j \rangle}, \quad (26)$$

where \hat{I}_j is our estimate of the sky intensity at each sky coordinate and again we assume calibrated gains $g_p(\vec{r}) = 1$. Note that this looks very similar to Eq. 19; the definition of the input and output coordinates are the same. If we choose a regular sampling of the discrete sky coordinates r_j in lmn coordinates while assuming negligible curvature of the sky ($\sqrt{1-l^2-m^2} \simeq 0$) and express the antenna baselines \vec{b}_n into the familiar frequency-dependent uvw frame we obtain:

$$\hat{I}[l, m] = \sum_u \sum_v V[u, v] e^{-2\pi i (ul+vm)}, \quad (27)$$

where $V[u, v]$ is the map of samples in the uv plane with sample positions given by the baseline vectors and sample strength given by V . Thus \hat{I} is the familiar *dirty image* often created as an intermediate step before deconvolution by state-of-the-art

radio interferometry imaging software such as WSClean. Deconvolution removes an effect called the point spread function (PSF) which is determined by the baseline geometry \vec{b}_n :

$$I_j^{\text{PSF}} = \sum_n^{N_A \times N_A} e^{-2\pi i \langle \vec{b}_n, \vec{r}_j \rangle}, \quad (28)$$

The back-projected image can be represented as the convolution of the true sky image I^{sky} with the PSF:

$$\hat{I} = I^{\text{PSF}} * I^{\text{sky}} \quad (29)$$

The target “clean” image is constructed by iteratively adding components to the initially empty model image $B_k \in \mathbb{R}^{N_{\text{sky}}}$, where components are selected using the residual $R_k \in \mathbb{R}^{N_{\text{sky}}}$. For example, if we use a dirac delta δ_j located at sky coordinate j for our component, then

$$\begin{aligned} R_k &= \hat{B} - \Psi^* B_{k-1} \Psi \\ B_k &= B_{k-1} + \alpha \delta_j, \quad \text{where } j = \operatorname{argmax}_j R_k[j] \end{aligned}$$

where α is some multiplicative gain factor. The iterations are halted when the current iterate is considered good enough, for example when the residual noise is smaller than some predefined threshold or after a fixed number of iterations. With enough iterations $B_{k \rightarrow \infty}$ will satisfy the least-squares minimization problem of Eq. 8, with additional implicit regularization provided by the component model.

The estimate from Bluebird \tilde{B} gives us a least-squares solution without any cleaning iterations. This makes \tilde{B} a useful replacement for \hat{B} for deconvolution-free imaging, which is foreseen for DSA-2000 (Hallinan et al., 2019). However, unlike B_k , \tilde{B} is constructed without any regularization terms, and still includes the effect of the PSF. This can easily be seen by comparing Equations 19 and 26: both expressions map N_A^2 samples at coordinates \vec{b}_n in the uvw plane to N_{sky} coordinates in the sky. The discrete \vec{b}_n sample coordinates create the PSF, but the sample values themselves change. Bluebird’s construction of \tilde{B} use the Gram-corrected visibilities used by Bluebird V' , and the back-projection \hat{B} uses the instrument visibilities $V = G_\Psi V'$, from the generalized eigenvalue problem.

Note that if we approximate the Gram matrix as the identity matrix $G_\Psi = \mathbb{I}$ then the back-projection and Bluebird least-squares estimate converge: $\hat{B} = \tilde{B}$ and $\hat{I} = \tilde{I}$. Many modern interferometers are implicitly designed such that the off-diagonal terms of the Gram matrix are be small, and thus \hat{I} is a reasonable approximation of the least-squares solution \tilde{I} . However, for instruments with redundant baselines or low frequencies, the off-diagonal terms are larger, and the Gram matrix has a stronger effect, as discussed in Appendix A.

2.9. Complexity analysis

For a given timestep and frequency band, the eigenvalue decomposition can be computed in $\mathcal{O}(N_A^3)$ operations. The computational cost of the decomposition does not contribute significantly to the overall computation time because N_A remains small; SKA-Mid in South Africa is expected to have

$N_A = 197$ dishes, and SKA-Low in Australia is expected to have $N_A = 512$ stations. Compared to the imaging steps of the algorithm the execution time for the eigenvalue decomposition is small, as shown in Section 5. For an observation with N_A dishes or stations, T timesteps, and F frequency bands, the computation time of the eigenvalue decomposition scales as $O(T F N_A^3)$.

For Standard Synthesis, the $N_A \times N_{\text{sky}}$ terms of ϵ_{aj} must be evaluated with a sum over N_A elements, the same computational cost as a direct Fourier transform. The computational complexity scales as $O(T F N_{\text{sky}} N_A^2)$. Unlike N_A , N_{sky} often has extremely large values.

The algorithmic complexity of the 3D type-3 NUFFT is (Kashani et al., 2023):

$$O((N_{\text{in}} + N_{\text{out}}) |\log \epsilon|^3 + N_{\text{out}} + N_{\text{mesh}} (\log N_{\text{mesh}} + 1)), \quad (30)$$

where N_{in} is the number of input points, N_{out} is the number of output points, ϵ is the user-requested accuracy parameter, and N_{mesh} is the uniform sampling which depends on the distribution of the input and output points. For NUFFT Synthesis we can stack our visibility samples across timesteps to obtain $N_{\text{in}} \propto N_A^2 T$ input samples, and similarly stack our N_A eigenvectors across $N_L \leq N_A$ levels. Then, using the type-3 NUFFT for F frequency channels has a leading order computational complexity of:

$$O(F N_L ((N_A^2 T + N_{\text{pix}}) |\log \epsilon|^3 + N_{\text{sky}} + N_{\text{mesh}} (\log N_{\text{mesh}} + 1))). \quad (31)$$

Thus the the T and N_{sky} scaling is decoupled, improving the performance of NUFFT Synthesis compared to Standard Synthesis.

We can furthermore reduce the dependence on F by stacking different frequency samples into the input points to the type-3 NUFFT, thus performing multi-frequency-synthesis. This functionality is not included in the current implementation of Bluebild, but is planned for a future release.

2.10. Previous implementations

A Python implementation of Bluebild currently exists on GitHub,² which includes extra software modules for reading in astronomical data, creating simulated data, interpolating output from the sphere to the plane, and writing output to the FITS file format (Pence et al., 2010).

3. Bluebild Imaging++

Bluebild Imaging++ (BIPP) is an HPC implementation of Bluebild based on the Python implementation by Kashani (2017), where the core Bluebild algorithm has been rewritten in C++. The BIPP library features interfaces to C++, C and Python and is designed with seamless GPU acceleration in mind. An additional Python module offers data preprocessing functionality for common input formats used in radio astronomy. The initial release of BIPP targets non-distributed computations only, but MPI support is planned for a later stage. The source code is publicly available on GitHub³.

N_{eig}	:	Number of requested eigenvalues.
N_f	:	Number of filters.
$S \in \mathbb{C}^{K \times K}$:	Visibility matrix.
$W \in \mathbb{C}^{N_A \times K}$:	Beamforming matrix.
$P_{\text{icrs}} \in \mathbb{R}^{N_A \times 3}$:	Stacked antenna positions in ICRS coords.
$P_{\text{uvw}} \in \mathbb{R}^{N_A^2 \times 3}$:	Stacked UVW coordinates.
$X_{\text{pix}} \in \mathbb{R}^{N_{\text{pixel}} \times 3}$:	Stacked image pixel coordinates.
$I \in \mathbb{R}^{N_i \times 2}$:	Stacked eigenvalue partition intervals of form [min, max].

Table 1: Input variables to the BIPP imaging handle. K is equivalent to N_A if beamforming is not used.

3.1. Interface

The interface to BIPP is structured around two types. A *Context*, which holds any reusable resources such as memory for either CPU or GPU processing, and an imaging handle called *StandardSynthesis* or *NUFFTSynthesis*, depending on which Bluebild image synthesis strategy is used.

An imaging handle can iteratively collect input data at each time step for a given set of filters and partitioning applied to eigenvalues. Through shared use of a *Context*, multiple imaging handles can share resources to reduce overall consumption. When using a GPU as a processing unit, most input data can be located in the host or device memory. BIPP will automatically transfer any data to device memory or vice versa as required. When using CPU processing, BIPP can utilize any LAPACK and BLAS compatible library for solving the eigenproblem and linear algebra operations.

For computing the NUFFT, FINUFFT (Barnett et al., 2019) is used. On GPU, BIPP relies on CUDA for Nvidia hardware and HIP for AMD hardware. With either programming framework, the corresponding BLAS and LAPACK libraries cuBLAS, cuSOLVER, hipBLAS or MAGMA (Tomov et al., 2010) are utilized, in addition to the cuFINUFFT library, for which a special fork with the required transform type and HIP support is available⁴.

3.2. Input data

BIPP uses a single function to process all data from a given single time step to enable better usage of GPU acceleration and overall interface simplicity. In the initialization stage, an imaging handle requires the coordinates for each pixel, the set of filters to apply to the eigenvectors, and the number of expected eigenvalue partitions in the form of intervals. The *collect* function expects the input shown in Table 1 in column-major memory layout for a given number of antennas N_A , beams K , and eigenvalue interval partitions N_i . Aside from the user-defined N_{eig} and I , all of these quantities can be extracted from real or simulated observations. BIPP is configured to read these quantities from standard CASA MeasurementSet (Kemball and Wieringa, 2000) files.

²<https://github.com/imagingofthings/pypipeline>

³<https://github.com/epfl-radio-astro/bipp>

⁴<https://github.com/AdhocMan/cufinufft/tree/t3.d3>

3.3. Standard Synthesis

Our implementation of the Standard Synthesis algorithm described in Section 2.4 is described in Algorithm 1. It uses a custom kernel for computing Eq. 15 for each pixel, interval and filter, such that the number of complex exponential evaluations is minimized as shown in Algorithm 2.

Algorithm 1 Standard Synthesis

```

1: procedure COLLECT( $N_{\text{eig}}, W, S, I, P_{\text{icrs}}, X_{\text{pix}}$ )
2:    $G \leftarrow$  Compute Gram matrix ( $W, P_{\text{icrs}}$ )
3:    $\alpha, \lambda \leftarrow$  Generalized eigenvalue decomposition ( $S, G$ )
4:    $\alpha, \lambda \leftarrow$  Select  $N_{\text{eig}}$  largest eigenvalues ( $\alpha, \lambda$ )
5:    $E \leftarrow$  GEMMEXP( $\alpha, W, P_{\text{icrs}}, X_{\text{pix}}$ )
6:   for  $n_f \in \{1, \dots, N_f\}$  do
7:      $\lambda_f \leftarrow$  Apply filter ( $n_f, \lambda$ )
8:     for  $n_i \in \{1, \dots, N_i\}$  do
9:        $K \leftarrow$  Indices of eigenvalues in interval  $I^{(n_i)}$ 
10:       $B^{(n_i, n_f)} \leftarrow B^{(n_i, n_f)} + \sum_{i \in K} d_f^{(i)} E^{(i)}$ 
11:    end for
12:  end for
13:  Store  $B$ 
14: end procedure

```

Algorithm 2 GEMMEXP kernel

```

1: procedure GEMMEXP( $\lambda, \alpha, W, P_{\text{icrs}}, X_{\text{pix}}$ )
2:    $U \leftarrow WA$ 
3:   for  $n_p \in \{1, \dots, N_{\text{pixel}}\}$  do
4:      $R \leftarrow 0$ 
5:     for  $n_a \in \{1, \dots, N_A\}$  do
6:        $p \leftarrow e^{i \frac{2\pi}{\lambda} (P_{\text{icrs}}^{(n_a)} \cdot X_{\text{pix}}^{(n_p)})}$ 
7:       for  $n_e \in \{1, \dots, N_{\text{eig}}\}$  do
8:          $R^{(n_e)} \leftarrow R^{(n_e)} + p U^{(n_a, n_e)}$ 
9:       end for
10:    end for
11:    for  $n_e \in \{1, \dots, N_{\text{eig}}\}$  do
12:       $E^{(n_e, n_p)} \leftarrow E^{(n_e, n_p)} + \|R^{(n_e)}\|^2$ 
13:    end for
14:  end for
15:  Return  $E$ 
16: end procedure

```

3.4. NUFFT Synthesis

We also implement the NUFFT Synthesis algorithm described in Section 2.5. However, direct evaluation of the N complex terms of equation 19 would involve computing exponential sums that naively require $O(N_{\text{baseline}} N_{\text{pixel}})$ effort. Instead, the FINUFFT library (Barnett et al., 2019) approximates the coefficients to within user-specified relative tolerance ϵ , in close to linear time in N_{baseline} and N_{pixel} . As neither the antenna baseline coordinates nor 3D sky pixel coordinates are uniformly distributed, we use the type-3 (nonuniform to nonuniform) NUFFT.

The first step is to rescale the 3D coordinates b_n to lie within $[-\pi, \pi]^3$ with dilation factors γ_i . We then write equation 19 as:

$$\tilde{B}_{\text{pix}} = \sum_n^N V_n' e^{i x_{\text{pix}}' b_n'}, \quad (32)$$

where $x_{\text{pix}}^{(i)} = \gamma_i x_{\text{pix}}$ and $b_n^{(i)} = \gamma_i b_n$. These rescaled baseline coordinates are then spread onto a fine regular grid b_x using a periodized kernel such that

$$b_x = \sum_n^N V_n \phi(x_1 h_1 - b_n^{(1)}, x_2 h_2 - b_n^{(2)}, x_3 h_3 - b_n^{(3)}), \quad (33)$$

where h_i is the fine grid spacing and ϕ is the normalized and periodized ‘‘exponential of semicircle’’ kernel from FINUFFT. The user-requested tolerance ϵ sets the kernel width and sampling. These b_x can be treated as Fourier series coefficients, and we can evaluate this series at rescaled target points using the type-2 NUFFT (uniform to nonuniform):

$$b_{\text{pix}} = \sum_x b_x e^{i x (h_i \gamma_i x_{\text{pix}}^{(i)})}. \quad (34)$$

Lastly, in order to compensate for the spreading step, a diagonal correction is needed:

$$\tilde{B}_{\text{pix}} = p_{\text{pix}} b_{\text{pix}}, \quad (35)$$

where the correction factors p_{pix} come from samples of the kernel Fourier transform. The grid size of the FFT coordinates b_p scales according to the kernel and the input dimensions b_n .

The cuFINUFFT library (Shih et al., 2021) includes implementations for the type-1 and type-2 NUFFT but not for type-3. We use a modified version of cuFINUFFT, where we implement the missing transform type. The procedure for the full image synthesis is shown in Algorithm 3.

Algorithm 3 NUFFT Synthesis

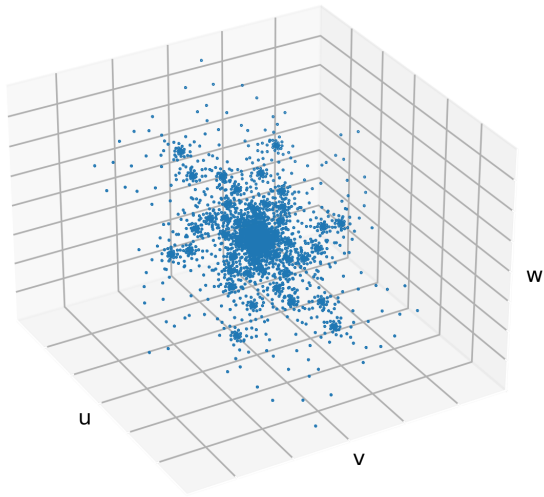
```

1: procedure COLLECT( $N_{\text{eig}}, W, S, I, P_{\text{icrs}}, P_{\text{uvw}}, X_{\text{pix}}$ )
2:    $G \leftarrow$  Compute gram matrix ( $W, P_{\text{icrs}}$ )
3:    $\alpha, \lambda \leftarrow$  Generalized eigenvalue decomposition ( $S, G$ )
4:    $\alpha, \lambda \leftarrow$  Select  $N_{\text{eig}}$  largest eigenvalues ( $\alpha, \lambda$ )
5:   for  $n_f \in \{1, \dots, N_f\}$  do
6:     for  $n_i \in \{1, \dots, N_i\}$  do
7:        $\alpha_I, \lambda_I \leftarrow$  Eigenvalues / vectors in interval  $I^{(n_i)}$ 
8:        $\lambda_f \leftarrow$  Apply filter ( $n_f, \lambda_I$ )
9:        $V \leftarrow \alpha_I \text{DIAG}(\lambda_f) \alpha_I^H$ 
10:       $B^{(n_i, n_f)} \leftarrow B^{(n_i, n_f)} + \text{NUFFT}(V, P_{\text{uvw}}, X_{\text{pix}})$ 
11:    end for
12:  end for
13:  Store  $B$ 
14: end procedure

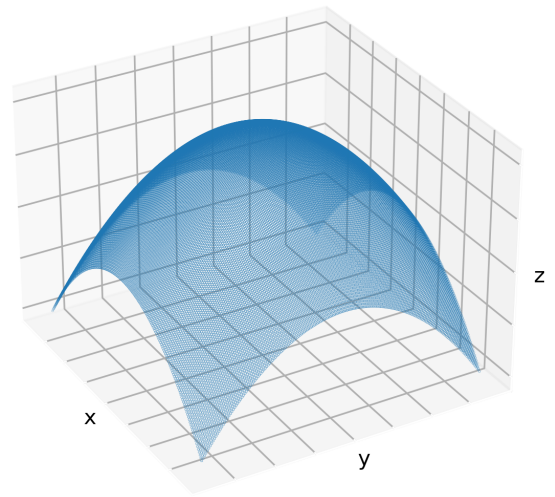
```

3.4.1. Domain Partitioning

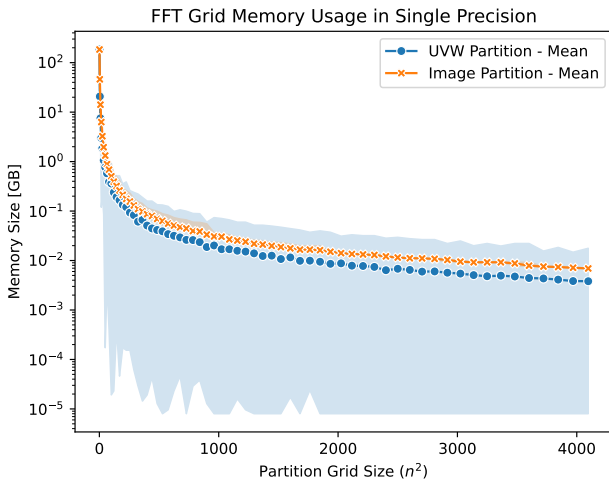
Computing a NUFFT requires spreading the nonuniform points onto a uniform 3D grid, allowing us to calculate the FT



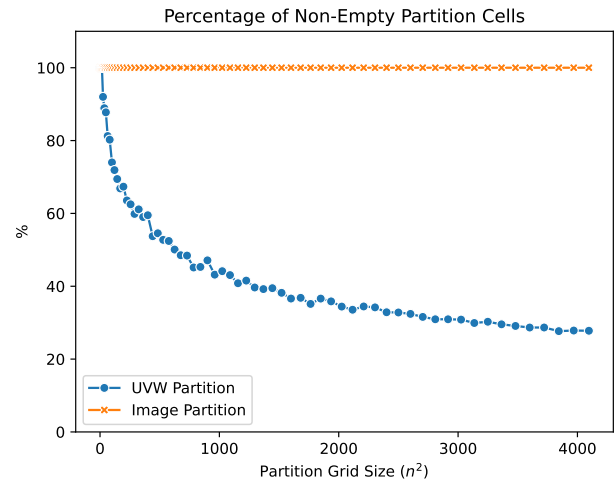
(a)



(b)



(c)



(d)

Figure 1: Domain partitioning of the input uvw (a) and output image pixel (b) coordinates for a simulated SKA-Low antenna array. (c) shows the mean memory size of the uniform FFT grid used for computing the NUFFT for a domain partition grid of size $(n, n, 1)$. The coloured area indicates the total spread between the minimum and maximum size. (d) shows the fraction of non-empty cells in the partition grid.

using an implementation of the Fast Fourier Transform. The size of the grid is directly proportional to the extent of the input and output coordinates. Therefore, the efficiency of an NUFFT approximation compared to the direct evaluation of the sum in Equation 19 depends on the spatial distribution of the input and output.

Tightly clustered data is typically most suited for NUFFTs. However, data with multiple clusters of input coordinates, such as certain antenna configurations used in radio astronomy, can be sub-optimal. In some cases, the required grid size may even exceed the available system memory.

To optimize the NUFFT performance, we implement spatial domain partitioning of the input and output data which splits a single NUFFT into multiple independent NUFFTs, such that the FFT grid size of each individual transform can be kept as small as possible, a similar strategy leveraged by [Kashani et al. \(2023\)](#). For input partitioning into I domain cells, this is equivalent to splitting the sum for each pixel into multiple sums:

$$\tilde{B}_{\text{pix}} = \sum_{n=1}^{N_I} V'_n e^{ix'_{\text{pix}} \cdot b'_n} + \dots + \sum_{n=N_{I-1}+1}^{N_I} V'_n e^{ix'_{\text{pix}} \cdot b'_n}. \quad (36)$$

When combined with output partitioning into O domain cells, the total number of NUFFTs is $O \times I$, where the pair-wise combination of input and output domain cells provides the input and output of a NUFFT.

We implemented domain partitioning using a regular 3D grid for both input and output. Figure 1 shows the results for simulated SKA-Low data with partitioning of the input UVW domain and output image domain. The input data consists of clustered points with some individually scattered around the domain, while output points are evenly spaced on a curved surface.

In Figure 1c, the memory usage per FFT is shown using a partitioning grid of size $(n, n, 1)$. For output partitioning of the more evenly spaced points, there is barely any difference in FFT grid size between each domain cell. In contrast, there is a wide variability in FFT grid size for the input UVW partitioning. This is also reflected in Figure 1d, which shows the percentage of domain cells containing any data points. For large partition grid sizes, as little as 30% of the domain cells require the computation of a NUFFT, which may, therefore, reduce the total number of operations required. However, a NUFFT will also require the spreading of input data and interpolation to output data, which only partially benefit from a smaller FFT grid size.

Whether domain partitioning provides a performance benefit is, therefore, highly dependent on the input and output distribution. It does, however, provide an avenue for parallelization and, as shown in Figure 1c, can reduce memory usage from over 200 GB to less than 1 GB.

3.5. Image weighting

BIPP can support “natural” and “uniform” image weighting by applying appropriate weights to the input visibilities before eigenvalue decomposition. For “natural” weighting, no additional weights are applied to the image. The system noise

is smallest in this case, but resolution and sidelobe noise are worse. For “uniform” weighting, we calculate the sampling density function on a grid in uv space with $\Delta u = \Delta v = 1/\text{FoV}$. Each visibility is then weighted with the inverse of its sampling density function. Unless otherwise noted, the results in Sections 4, 5, and 6 are created using natural image weighting.

3.6. Current Limitations

As discussed in Section 2.8, the images produced by the Bluebuild algorithm do not include any regularization. As such, the images produced by BIPP are comparable to the “dirty” images produced by standard radio astronomy imaging algorithms, i. e. the true image of the sky is convolved with the instrument’s point spread function ([Taylor et al., 1999](#)). Additional deconvolution would be required to produce a comparable “clean” image. Nevertheless, the eigenvalue decomposition offers some interesting advantages, as discussed in Section 6.

BIPP assumes that the array contains calibrated omnidirectional antennas $g_p(\vec{r}) = 1$. Future developments will include an option to include a non-uniform instrument response.

Currently BIPP uses all baselines to reconstruct the image, even if those baselines provide a resolution higher than the imaging resolution. In other radio astronomical imaging libraries, these longer baselines are discarded to improve performance. The effect of baseline truncation must be kept in mind when comparing BIPP to other imaging software. An option for baseline truncation will be added in a future release.

Finally, while BIPP has been extensively validated against data files from MWA and LOFAR, as discussed in Section 4, we have not exhaustively tested input files from every telescope. To include beamforming as described in Section 2.7, BIPP reads in time-varying station element positions, which are not necessarily structured the same in CASA MeasurementSet files from different telescopes.

4. Validation

To validate our implementation of Bluebuild, we compare the outputs of BIPP with the outputs of the original Python implementation. Furthermore, we compare the consistency of our implementations of Standard Synthesis with NUFFT synthesis and the CPU and GPU implementations. In total, we compare five different implementations of the Bluebuild algorithm:

- `BluebuildSsCpu`: Original implementation in Python of the Standard Synthesis algorithm from the `pypeline` library ([Kashani, 2017](#)), running on CPU
- `BippSsCpu`: C++ implementation of the Standard Synthesis algorithm, running on CPU
- `BippSsGpu`: C++ implementation of the Standard Synthesis algorithm, running on GPU
- `BippNufftCpu`: C++ implementation of the NUFFT Synthesis algorithm, running on CPU
- `BippNufftGpu`: C++ implementation of the NUFFT Synthesis algorithm, running on GPU

For the validation tests, the NUFFT user-requested tolerance ϵ is set to 10^{-5} .

Furthermore, we compare the BIPP output images to those produced with two reference packages in the field: WSClean (version 3.4, using the `wgriddler` griddler with its default accuracy of $1e-4$) (Offringa et al., 2014) and the `tclean` task from CASA (version 6.6.3-22, using the `wproject` griddler, setting the number of distinct `w`-values to -1, letting this parameter to be automatically defined by CASA) (McMullin et al., 2007). For both of these imaging libraries, the number of cleaning iterations is set to zero. Thus, we only compare dirty images \hat{I} to BIPP outputs \tilde{I} .

4.1. Dataset

For our validation checks, we use OSKAR (Mort et al. (2010), release 2.8.3) to create four simulated SKA-Low telescope observations with a configuration of 512 stations and variable field-of-view (FoV) of 17, 34, 68 or 136 arcmin. We create a radio sky with 9 point sources of 1 Jy spread over a regular grid⁵ over the FoV. 50 time steps are generated spread over an observing period of 6 hours.

The simulated visibility data are then processed with CASA, WSClean and all five implementations of Bluebild. In all cases, no cleaning is performed, and Bluebild LSQ images \tilde{I} are compared to the CASA and WSClean so-called "dirty" images. To ensure a fair comparison, the resolution is fixed to 4 arcsec, so to prevent the visibility truncation of WSClean and CASA as discussed in Section 3.6. This results in square images with 256^2 , 512^2 , 1024^2 and 2048^2 pixels.

These same datasets and imaging strategies are used for the performance benchmarks described in Section 5.

4.2. Impact of the energy clustering

For each of the five implementations of Bluebild we assess the impact of the eigenvalue partitioning (see Sect. 2.6) on image reconstruction. All eigenvalues (positive and negative) are considered, with no eigenvalue truncations, such that $N_{\text{eig}} = N_A$. Eigenvectors $\{\alpha_a\}$ with positive eigenvalues are clustered into 1, 2, 4, or 8 distinct energy levels, and all eigenvectors with negative eigenvalues are partitioned into a single separate layer. The resulting energy levels are summed together to create the complete LSQ image \tilde{I} .

For each implementation and each image size we assess the impact of the energy clustering by computing differences between images. Results are summarized in Table 2, which gathers, for each solution, the largest interval of differences between two energy levels over all image sizes. We emphasize here that Table 2 reports the worst-case scenarios for each implementation. We find that the energy clustering scheme has a negligible impact on the resulting image, as expected from Eq. 37. The errors observed are consistent with single-point floating precision used in the calculation for Standard Synthesis implementations and consistent with the tolerance $\epsilon = 10^{-5}$ tolerance for NUFFT implementations, as expected.

⁵Sources were simulated to be located at the center of the pixels located at $1/8$, $4/8$ and $7/8$ of the image width on both images axes.

Solution	Im. width [pixel]	Levels	Maximal range [Jy/beam]	RMS [Jy/beam]
BluebildSsCpu	256	1 & 4	[-4.8e-7, 4.8e-7]	8.3e-8
BippSsGpu	2048	1 & 2	[-2.0e-6, 7.2e-7]	2.4e-8
BippSsCpu	2048	1 & 2	[-2.1e-6, 7.7e-7]	2.4e-8
BippNufftGpu	256	1 & 8	[-3.4e-5, 2.6e-5]	1.0e-5
BippNufftCpu	256	1 & 8	[-1.3e-6, 1.5e-6]	2.7e-7

Table 2: Maximal range of intensity differences reported for each implementation of Bluebild when comparing images obtained using different number of energy levels for the clustering of the eigenvalues.

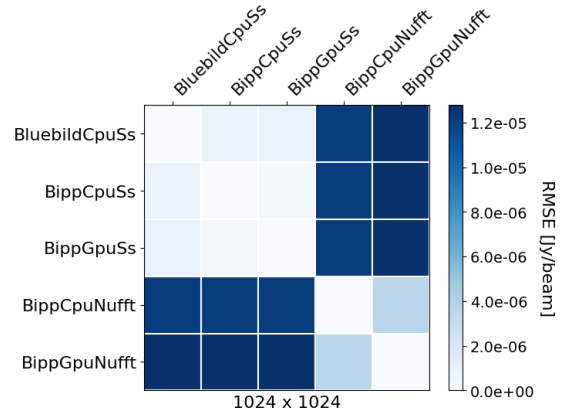


Figure 2: Inter-solution consistency between the different implementations of Bluebild for images of 1024×1024 pixels and produced by combining all positive eigenvalues into a single layer. Similar results are obtained when clustering eigenimages into 2, 4 or 8 positive energy levels, see Section 2.6.

4.3. Consistency between implementations

We evaluate the consistency of the images produced by our five implementations of Bluebild. Consistency here is measured as the RMS of pixel intensity differences between two images, referred to as the RMS error or RMSE. Figure 2 presents the inter-solution consistency for the 1024^2 pixel image.

The overall agreement between all solutions is excellent, with a quasi perfect agreement between the three Standard Synthesis solutions while the maximum RMSE of only $1.28e-05$ Jy/beam is found between the `BippNufftGpu` and Standard Synthesis. Agreement between `BippNufftCpu` and the Standard Synthesis solutions reduces to $1.22e-05$ Jy/beam while the agreement between `BippNufftGpu` and `BippNufftCpu` is around $3.61e-06$. These numbers were obtained for 1024^2 pixel images.

4.4. Recovering simulated point sources

In addition to checking the per-pixel consistency between imaging solutions, we also evaluate the ability of the three packages CASA, WSClean, and BIPP to recover properties of the simulated point sources in our validation dataset. We calculate the distance (in pixels) between recovered and simulated sources' positions and the intensity of the recovered sources compared to the simulated ones (1 Jy everywhere). In Figure 4 we show the outputs of CASA, WSClean, and BIPP imaging the

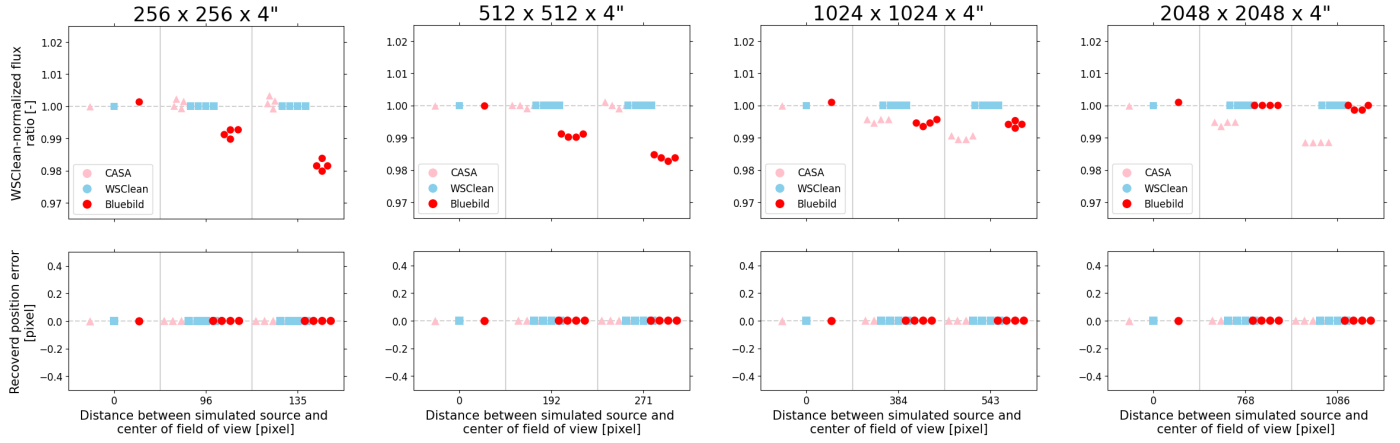


Figure 3: Top plots: recovered intensities relative to the flux measured in the WSClean image and bottom plots: distance between the recovered source positions and the simulated ones, in pixels, all plotted against the distance in pixels to the centre of the field of view. The size of the images increases from the left to the right from 256 to 2048 pixels. The Bluebild solution (in red) was obtained with BIPP NUFFT GPU implementation. Inconsistency in recovered flux as a function of image size is likely due to gridding/interpolation effects because we use the maximum pixel value for the recovered intensity.

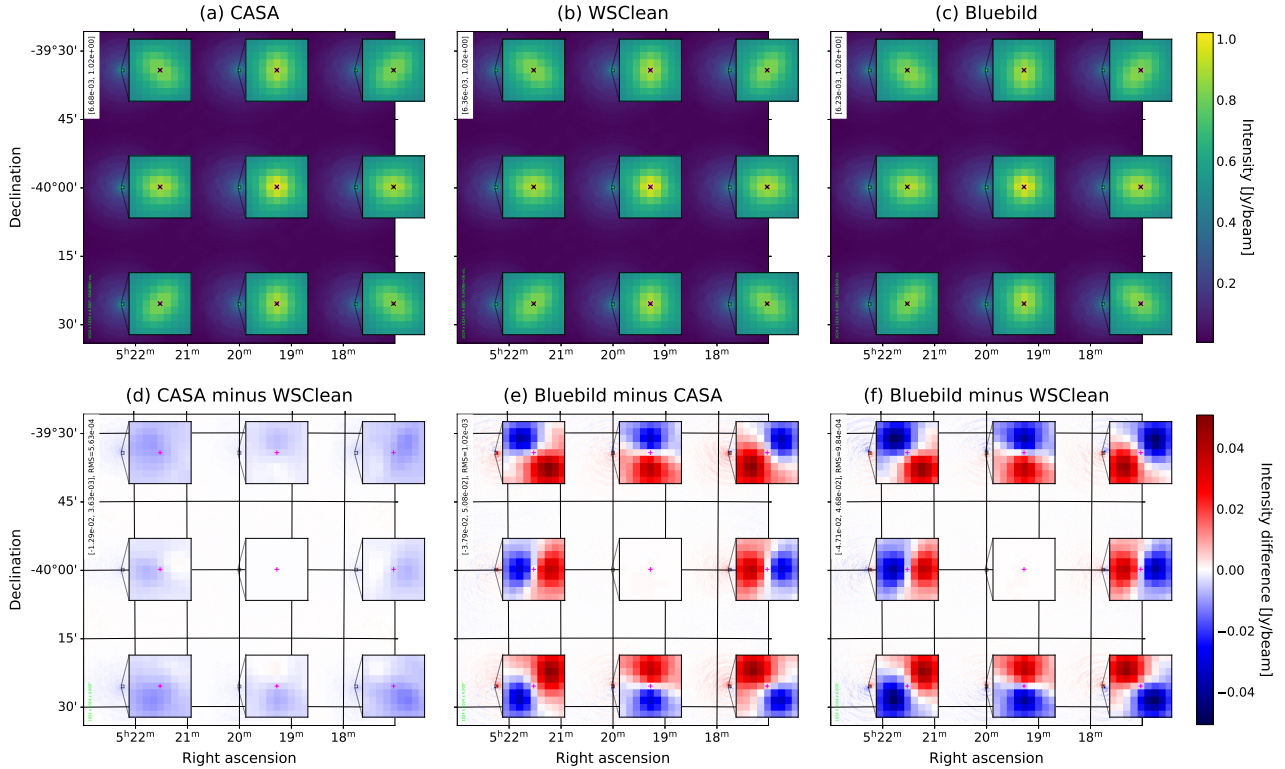


Figure 4: Recovered simulated 1 Jy point sources by CASA, WSClean and BIPP and differences between output images. Images are of $1024 \times 1024 \times 4''$ resolution. Pink crosses indicate the positions of the simulated sources whereas the black ones indicate the position of recovered sources, i.e. the position of pixel of highest intensity in the vicinity of the true position. The BIPP solution was obtained with the NUFFT Synthesis algorithm and running on GPU.

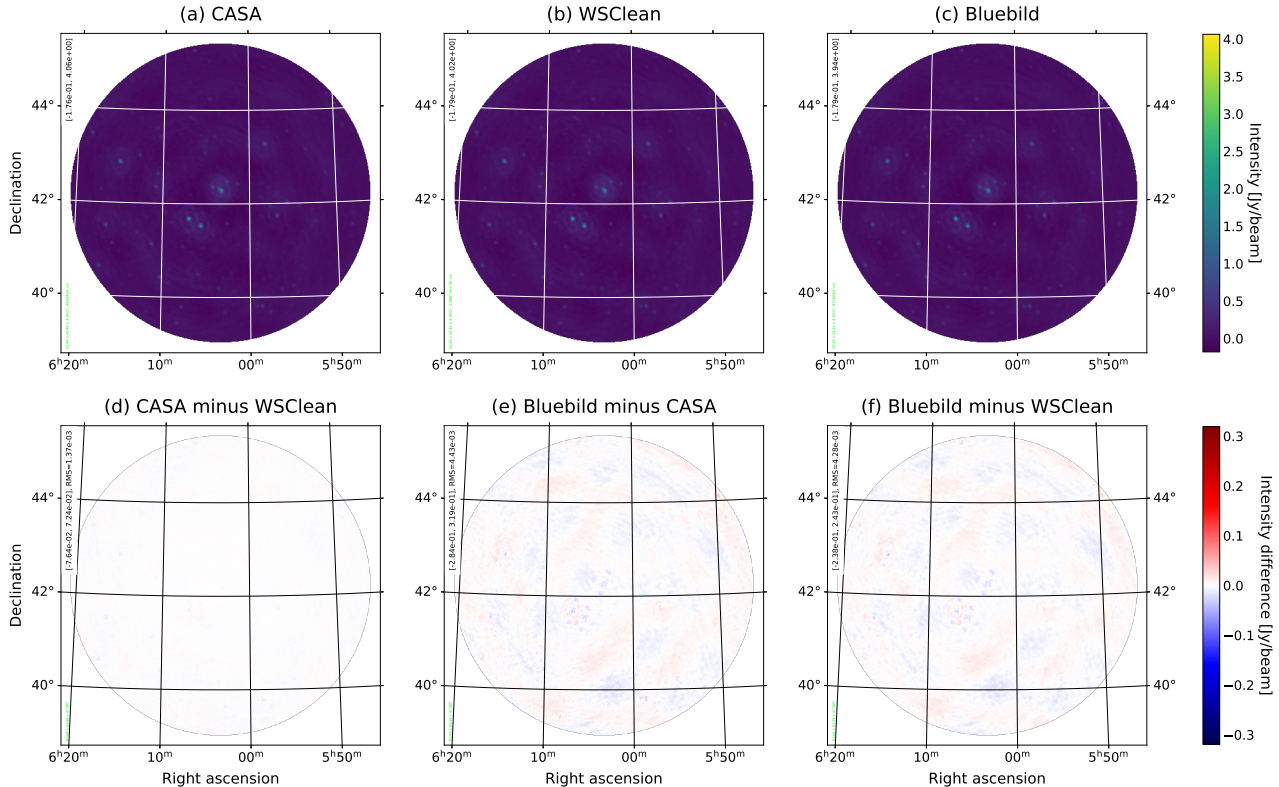


Figure 5: Top row: dirty maps produced with (a) CASA, (b) WSClean, (c) BIPP using real LOFAR data from the Toothbrush cluster RX J0603.3+4214 dataset from Pan et al. (2017). Images produced are 6144 by 6144 pixels of 4'' angular resolution. Bottom row: differences between the following pairs of dirty maps: (d) CASA minus WSClean, (e) BIPP minus CASA and (f) BIPP minus WSClean. Mask from the CASA solution was applied to the two others for a fair comparison.

same visibilities to create 1024^2 pixel images with 4'' resolution. Pink crosses indicate the true/simulated positions of the point sources, and dark crosses indicate their recovered positions, taken as the position of the pixel of highest intensity in the vicinity of the location of the simulated source (9×9 pixels square area centered on the source's true location).

Figure 3 provides a global summary of the recovery of the point sources for the `BippNufftGpu` solution for all image sizes. All three software packages recover consistent source positions and intensities. In the field comparisons in Figure 4 we see that the BIPP image has almost perfect agreement in the center of the FoV, but sources farther from the center are slightly offset with respect to the images reconstructed by CASA and WSClean, with offset increasing with distance. This is likely due to the use of the 3D NUFFT for imaging directly on the sphere instead of a w -term approximation. These sub-pixel offsets do not change the recovered source position.

4.5. Processing real LOFAR data

Finally, we also check the output of BIPP on real data collected by the Low-Frequency Array (LOFAR) telescope. We use dataset IV from Pan et al. (2017), a LOFAR observation of the ‘‘Toothbrush’’ cluster RX J0603.3+4214 from 36 stations over the period 2013-02-24-15:32:01.42 to 2013-02-25-00:09:24.51, resulting into 3,123 observation time steps. We use just a single frequency channel with central frequency of 130.2 MHz. Dirty images of 6144×6144 pixels of 2'' angular

resolution were computed with CASA and WSClean, and compared to the LSQ image \tilde{I} produced by BIPP. The BIPP solution was obtained with the `BippNufftGpu` implementation with a convergence criterion of $\epsilon = 10^{-5}$.

The results are shown in Figure 5. The overall similarity between the three solutions is excellent, with maximal differences at the 2.5% level found in the comparison between the CASA and BIPP located around the brightest source. CASA and WSClean images show the best agreement, with an RMSE of $1.65e-3$ Jy/beam. Differences between BIPP and the two other solutions are a bit more pronounced compared to the simulated dataset, with large scale light structures, resulting in larger RMSE of $4.92e-3$ (CASA) and $4.70e-3$ (WSClean). This is likely because this field is less sparse than the simulated dataset with only 9 sources.

4.6. LSQ Imaging

The differences between the BIPP and CASA/WSClean images is mostly driven by the different gridding algorithm that these software packages use for imaging. WSClean uses w-stacking (Offringa et al., 2014), CASA uses w-projection (Cornwell et al., 2008), and BIPP uses a 3D NUFFT of type 3 (non-uniform input to non-uniform output).

To disentangle these effects, we also evaluate the difference between the LSQ-consistent image \tilde{I} constructed by Bluebild with the back-projected dirty image \hat{I} , using the 3D NUFFT of type 3 to perform the gridding and FFTs in both cases. The

results for both the simulated data with 9 point sources and the LOFAR Toothbrush data are shown in Figure 6. As discussed in Section 2.8, the Gram matrix has a small effect if the instrument baselines are much larger than the observing wavelength, which is true for both of these datasets. The differences we see between \tilde{T} and \hat{T} are at the sub 0.1% level, which is smaller than the differences observed between CASA and WSCLEAN reconstructed images. The CASA - WSCLEAN RMS is 5.6×10^{-4} Jy/beam for the simulated SKA-Low data and 1.4×10^{-3} Jy/beam for the LOFAR data, which is larger than the RMS for the $\tilde{T} - \hat{T}$ residual of 1.1×10^{-4} Jy/beam and 8.29×10^{-5} Jy/beam, respectively.

5. Performance Tests

In this section we examine the computational performance of the five implementations of the Bluebird algorithm (i.e. BluebirdSsCpu, BippSsCpu, BippSsGpu, BippNufftCpu and BippNufftGpu as described in Section 4) to the reference packages CASA and WSClean. As in Section 4, we only compare the execution times for CASA and WSClean to create dirty images.

For the benchmark, we use the same sets of data as described in Section 4.1. We process 50 time steps of OSKAR simulated SKA-Low observations based on 512 observing stations. The pixel angular resolution was fixed to 4 arcsec while the size of the image was set to either 256^2 , 512^2 , 1024^2 or 2048^2 pixels, resulting in a varying FoV. For each of these image sizes, all five Bluebird implementations were run with 1, 2, 4 and 8 positive energy levels on top of a single negative energy level containing all of the negative eigenvalues. So, in total, our benchmark contains, for each image size, $4 \times 5 = 20$ Bluebird results.

All the computations were carried out using single-precision (32-bits) floating-point numbers. NUFFT partitioning for both uvw and image domains was set to (4, 4, 1), as described in Section 3.4.1. The code was compiled using the GCC v11.3.0⁶ and NVCC v11.8.89⁷ compilers.

Each solution is run with exclusive access to one of the large memory nodes of the GPU cluster of EPFL called Izar. Each node has 384 GB of DDR4 RAM, 2 Intel Xeon Gold 6230 CPUs running at 2.10 GHz with 20 physical cores each (one thread per physical core), and 2 NVidia V100 PCIe 32 GB GPUs. Multi-threaded regions of the code use the 40 CPU cores available. GPU-accelerated parts of the code use a single GPU out of the two available.

We analyse the times to solutions (TTS) and speedup factors (SF) obtained with the different BIPP implementations when compared to the reference Python implementation of Bluebird. Results are displayed in Figure 7 for 1 energy level (left) and 8 energy levels (right). Table 3 provides the speedup factors of all BIPP solutions, CASA and WSClean when compared to Bluebird in producing images. Table 4 presents the decomposition of the time to solution for the best performing BIPP solution, namely the BIPP NUFFT GPU implementation when

Solution	Speedup factors [-]							
	1 energy level				8 energy levels			
Image size	256 ²	512 ²	1024 ²	2048 ²	256 ²	512 ²	1024 ²	2048 ²
FoV [arcmin]	17	34	68	136	17	34	68	136
BippSsCpu	1.55	1.39	1.41	1.70	1.35	1.42	1.49	1.68
BippSsGpu	9.28	11.01	13.54	17.58	8.89	11.77	13.88	17.42
BippNufftCpu	1.64	3.95	13.40	45.27	0.49	1.27	4.27	13.29
BippNufftGpu	8.04	24.97	77.91	207.72	2.55	10.05	39.86	114.06
CASA	5.00	8.37	52.93	133.49	2.43	10.08	31.37	106.78
WSClean	4.42	13.27	49.57	230.47	3.94	14.06	50.21	222.03

Table 3: Speedup factors for BIPP, CASA and WSClean solutions compared to the reference Bluebird Python implementation to produce images with 256, 512, 1024 and 2048 pixels resolutions. BIPP speedups in the left part of the table were obtained, setting up 1 positive energy level, while on the right-hand side are given the speedup factors obtained when setting up 8 positive energy levels. The small differences observed for CASA and WSClean results between the 1 and 8 energy levels setups stem from instabilities inherent to using shared resources (CASA and WSClean were run by default along each solution).

constructing the LSQ image using only a single energy level. We notice the following results:

- NUFFT Synthesis has better scaling than Standard Synthesis, as expected from the complexity analysis in Section 2.9.
- Combining eigenvectors into distinct energy levels as discussed in Section 2.6 improves the performance of NUFFT Synthesis by reducing the number of calls to the NUFFT, but does not impact the performance of Standard Synthesis.
- BIPP GPU implementations outperform CPU implementations for both Standard Synthesis and NUFFT Synthesis.
- BippNufftGpu is the fastest imager for images with $N_{\text{pixel}} \leq 1024^2$, faster than both WSClean and CASA. However, the scaling appears to be better for WSClean and CASA and they perform better for larger image sizes.
- The eigenvalue decomposition takes up a very small part of the total execution time, as shown in Table 4.

Most of the execution time of the NUFFT GPU implementation is dominated by the 3D NUFFT. However, it would be possible to use w -projection or w -stacking to evaluate the DFT of the Gram-corrected visibilities in Equation 19, allowing more performant fPCA-based LSQ imaging for larger image sizes.

6. Scientific Applications

One of the unique aspects of BIPP is that the sky is reconstructed in distinct orthonormal eigenimages:

$$\tilde{T} = \sum_a \lambda_a |\epsilon_a|^2 = \sum_a \lambda_a |\Psi \alpha_a|^2. \quad (37)$$

Each eigenimage $|\epsilon_a|^2$ can be reconstructed from the corresponding visibility eigenvector α_a in parallel. As discussed

⁶<https://gcc.gnu.org/gcc-11/>

⁷<https://docs.nvidia.com/cuda/cuda-compiler-driver-nvcc/index.html>

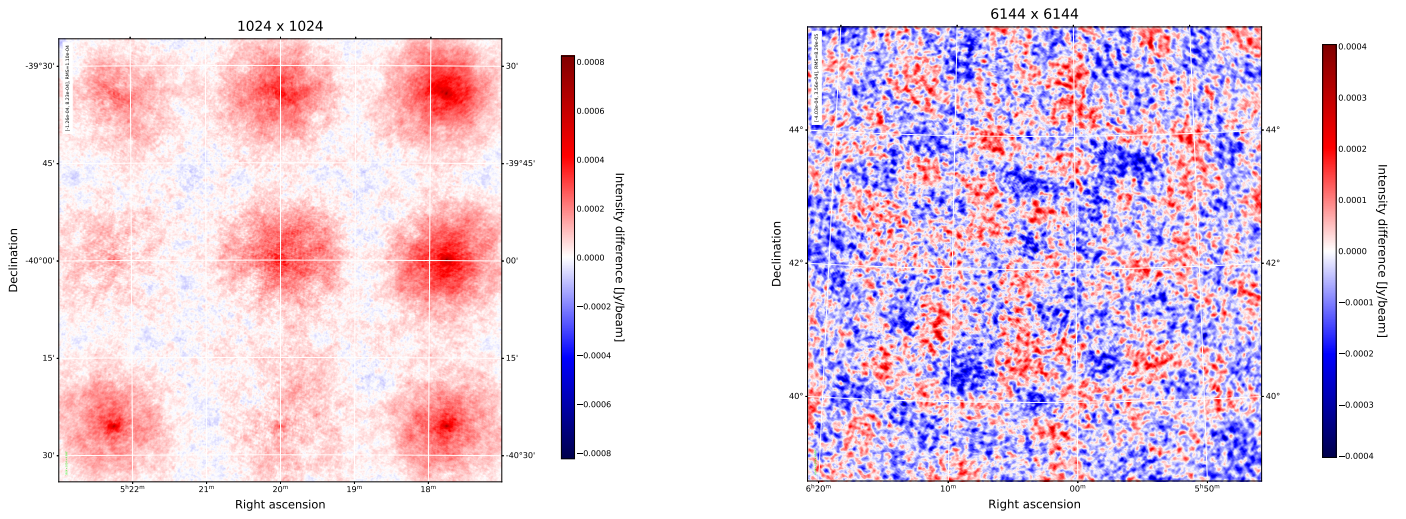


Figure 6: $\hat{I} - \tilde{I}$ for (left) simulated SKA-Low observation with 9 sources and (right) the Toothbrush cluster RX J0603.3+4214 LOFAR observation. Observed differences are at the sub 0.1% level, smaller than the differences observed between CASA and WSCLEAN.

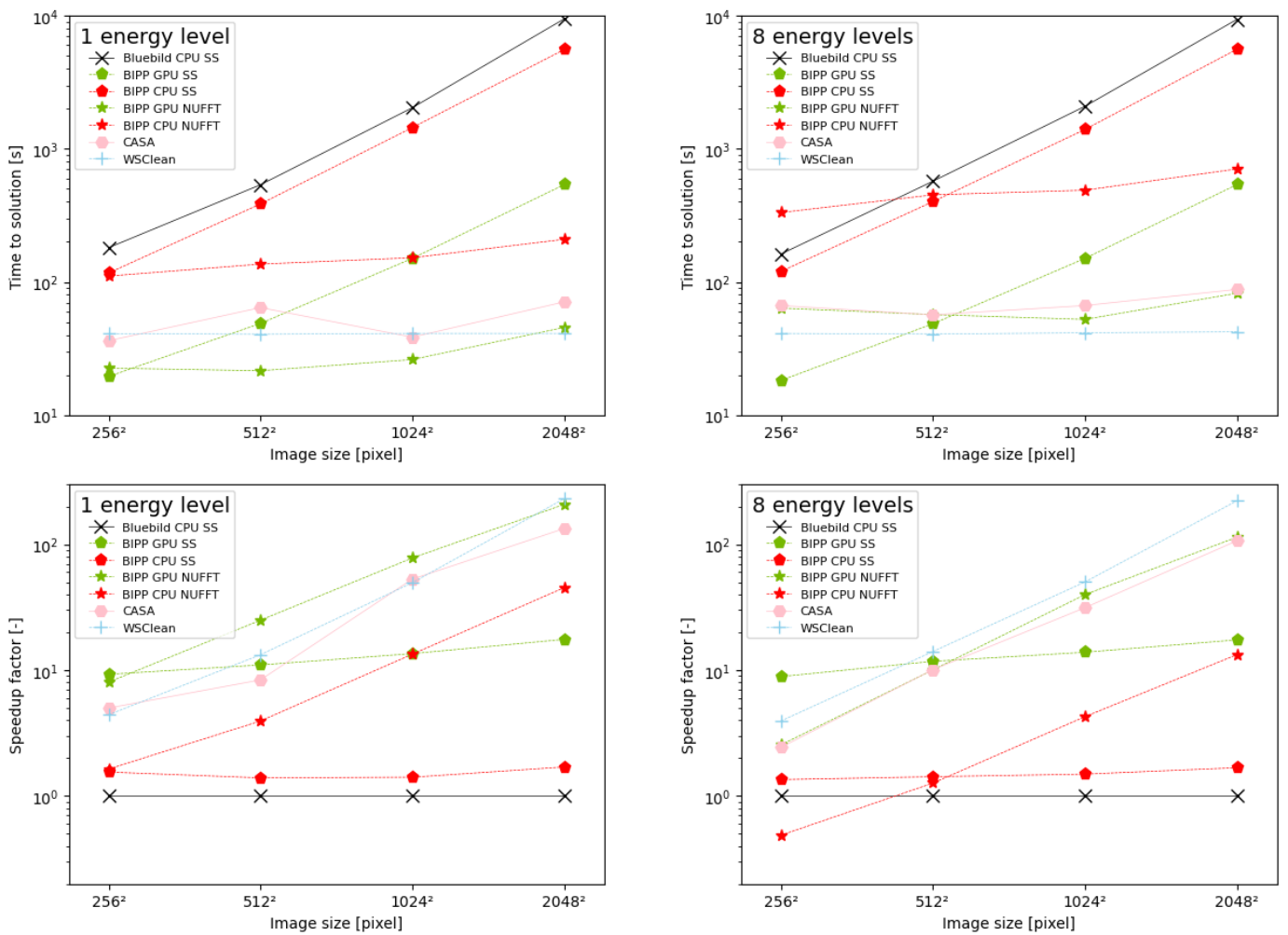


Figure 7: Top row: times to solutions when imaging with one or eight distinct energy levels. Bottom row: the corresponding speedup factors computed over the reference BluebildSsCpu solution.

Process	Time [s]	% Total
Total	45.57	100.0
Parameter estimation	4.42	9.7
Reading visibilities	1.91	4.2
Processing	2.50	5.9
Eigen decomposition	0.60	1.3
Imaging	41.03	90.0
Reading visibilities	1.84	4.0
Processing	39.19	86.0
Eigen decomposition	0.50	1.1
Other	0.12	0.3

Table 4: Decomposition of the times to solution for the BIPP NUFFT GPU solution obtained with a single positive energy level when generating a 2048 x 2048 pixel image from 512 stations. Parameter estimation is an optional preliminary imaging step that runs on a small subset of the input file before the full image synthesis.

in Section 2.6, these eigenimages and eigenvisibilities can be sorted and clustered by their eigenvalues λ_a , allowing for natural partitioning of energy in the radio sky into separate images.

This source separation is a unique benefit of the algorithm, and we present a few examples of this energy separation on real and simulated data. These examples use k -means clustering to cluster distinct λ_a into k energy levels.

6.1. Point sources

In Figure 8, we show an example of the energy level partitioning performed by BIPP on simulated point sources. We use the same SKA-Low observation configuration as described in Section 4.1, but we modify the sky model to have evenly spaced source flux of 1 Jy - 9 Jy. To primary beam correction is applied.

The reconstructed LSQ image and corresponding eigenvalue partitioning are shown in Figure 8. The LSQ image is shown in the upper left panel. Although the bottom left source has a true flux of 9 Jy, due to the primary beam it is reconstructed with a flux of ~ 7 Jy/beam. The energy partitioning creates distinct images of flux at different scales but there is some mixing of components between different levels— we can see for example that the brightest source is split into a ~ 5.5 Jy/beam source in Level 0 and a ~ 1.5 Jy/beam source in Level 1. Some sources are almost perfectly partitioned into their own levels, as seen in Levels 5, 6, 7, and 8. Levels 9 and above begin to contain artifacts consistent with noise.

6.2. Solar Limb Brightening

In Figure 9 we show an example of the source separation performed by BIPP on observed MWA data. The observation targets the quiet sun (Sharma and Oberoi, 2020) using Phase I of the MWA; meaning that 128 phased arrays observe free-free emission from the solar corona which is affected by anisotropic scattering and refraction due to the coronal medium. The resulting image has a field of view of 14.3 degrees. We zoom in on a 2.1 degree field of view centered on the sun in panels (a), (c) and (d) of Figure 9. The integration time for the observation is 10 seconds, with 0.5 second time steps. The central

frequency of observation is 216.94 MHz; further, the observation is composed of 64 channels of bandwidth $\Delta\nu = 40$ kHz between 215.68 MHz and 218.2 MHz.

We image this observation with BIPP, shown in Figure 9. We note the radially decreasing emission that is typical of radio images of the sun in Figure 9 (a). We reconstruct the image in two separate levels. The higher level (level 0; Figure 9 (c)) is almost identical to the summed least-squared image in the top-left panel of the same figure. However, the lower level (level 1; Figure 9 (d)) shows an interesting emission pattern focused on the solar limb. This emission is not evident in images reconstructed with CASA or WSClean, but is revealed through Bluebird’s eigenvalue decomposition.

We image a simulated solar observation (Figure 9 (a)) using OSKAR to validate our discovery of radio limb brightening emission from the sun, shown in Figure 10.

We simulate the solar free-free emission using the FORWARD (Gibson et al., 2016) software. This software uses a self-consistent Magnetohydrodynamic Algorithm outside a Sphere (MAS) coronal model. It then takes the temperature, electron density and magnetic field from input HMI Magnetograms and normalises these against photospheric values. Finally, it calculates the brightness temperature in various Stokes parameters. We calculate the corresponding visibilities using the MWA Phase I configuration with OSKAR.

Figure 10 (b) shows the summed BIPP least-squared image. We can see the radially decreasing, centre brightened solar emission, but not the fine structure present in the simulation itself.

However, we can observe this fine scale structure in the middle imaging level (level 1; Figure 10 (e)). Like the simulation, emission is primarily situated around the solar limb and is roughly two orders of magnitude weaker than the radially decreasing emission seen in the summed BIPP least-squares image. The presence of such features in the least-squared level 1 validates our observation of solar limb-brightening in the bottom-right panel of Figure 9. Finally the Figure 10 (f) shows the noise in level 2.

This example is particularly interesting, since it demonstrates both the denoising and the filtering properties of BIPP’s eigenvalue decomposition and k -means clustering.

6.3. Discussion

As discussed in Section 2.8, the Bluebird LSQ image \tilde{I} does not include any regularization, whereas the final image created by clean $I_{k \rightarrow \infty}$ satisfies the LSQ problem and includes regularization. If we wish to perform deconvolution on the output of BIPP, we can set $G_\Psi = I$ in the eigenvalue decomposition in Equation 13 to solve for the eigenpairs $\{\lambda'_a, \alpha'_a\}$:

$$V\alpha'_a = \lambda'_a\alpha'_a. \quad (38)$$

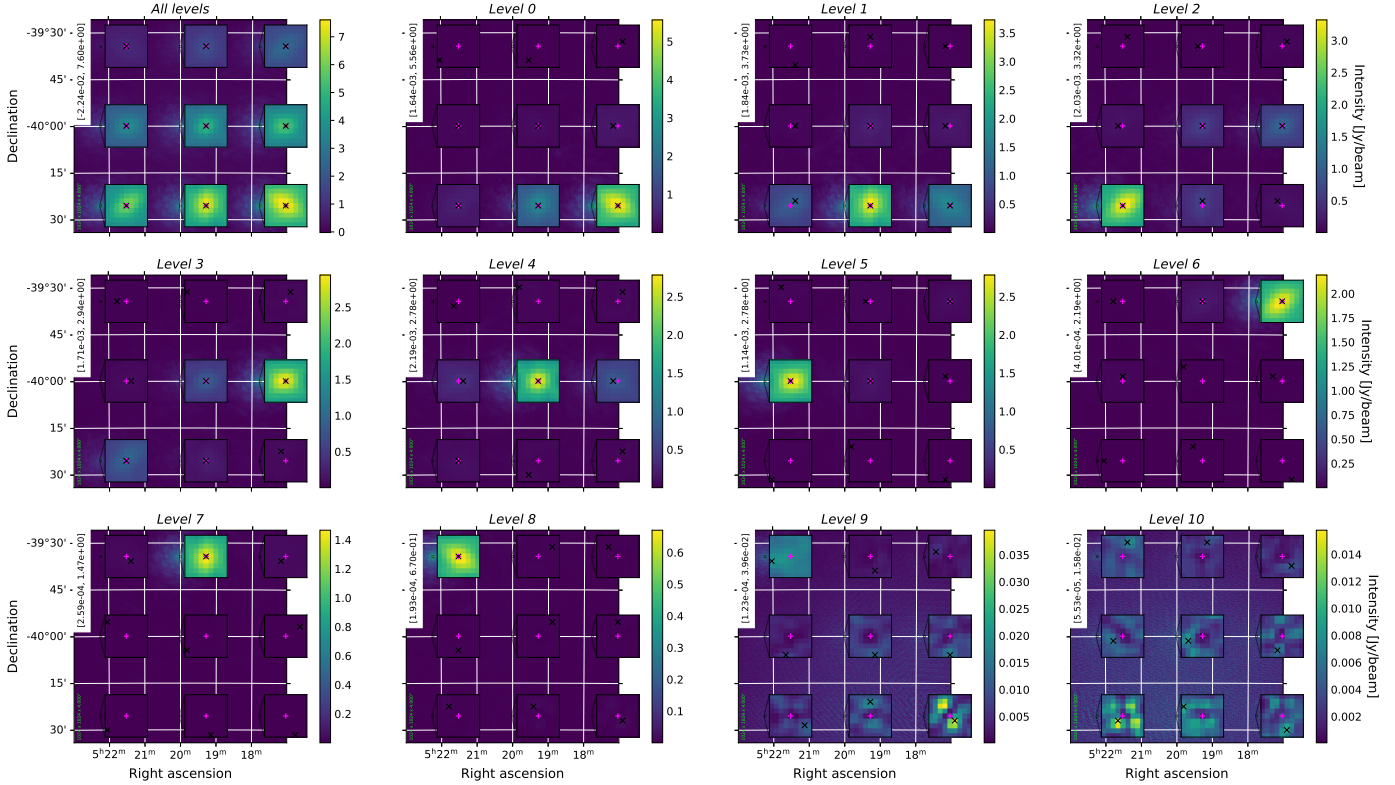


Figure 8: Simulated observation of 9 point sources with an SKA-Low configuration. The top left panel shows the LSQ image, and the other panels show the energy level partitioning in order of decreasing energy.

This gives us an eigendecomposition of the dirty image \hat{I} instead of \tilde{I} :

$$\hat{B} = \Psi V \Psi^* = \sum_a^{N_A} \lambda'_a \Psi \alpha'_a (\alpha'_a)^H \Psi^* \quad (39)$$

$$\hat{I} = \sum_a^{N_A} \lambda'_a \Psi |\alpha'_a|^2 \Psi^* \quad (40)$$

where $\hat{B}_{jj} = \hat{I}_j$.

Because for most interferometers $G_\Psi \approx I$, this is also a useful framework for interpreting the results of the decomposition in Sections 6.1 and 6.2. The fPCA gives us orthogonal visibility eigenvectors α'_a that can be linearly combined to create the dirty image \hat{I} . Each eigenvisibility $|\alpha'_a|^2$ should correspond to sources of energy or “components” corresponding to the eigenvalue λ'_a . This separation does not impose any prior on the morphology of the components, unlike CLEAN, but also does not apply any regularization so the different energy levels are still contaminated by the instrument PSF.

The eigenvalue decomposition is particularly useful for scientific applications that need to filter specific energy levels. Bright source peeling can be performed in visibility space by discarding the brightest eigenvisibilities $|\alpha'_a|^2$ before the image synthesis step.

The energy levels produced by BIPP could also be a useful input to AI-based deconvolution, as the dynamic range of each energy level is much smaller than the combined LSQ image.

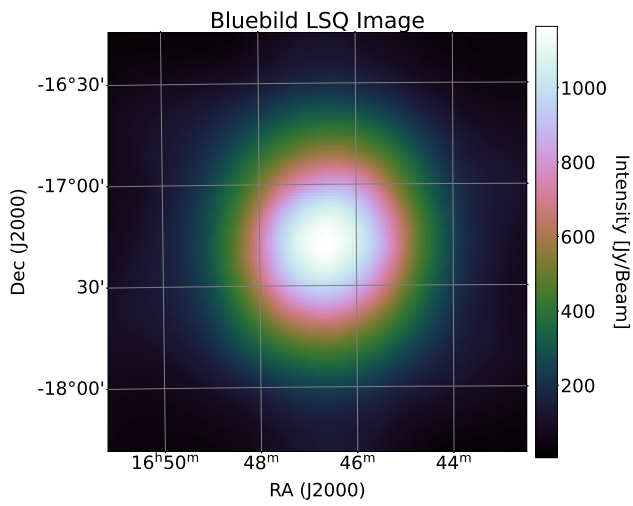
Regularization/cleaning could be performed independently and in parallel on each level, either in visibility space or image space, before combining the levels to create the cleaned LSQ image.

However, the decomposition offered by Bluebild is not always easily interpretable. The energy λ'_a does not necessarily correspond to the energy of a particular component. For example, in Figure 8 several point sources are split into multiple components in the same location across different energy levels.

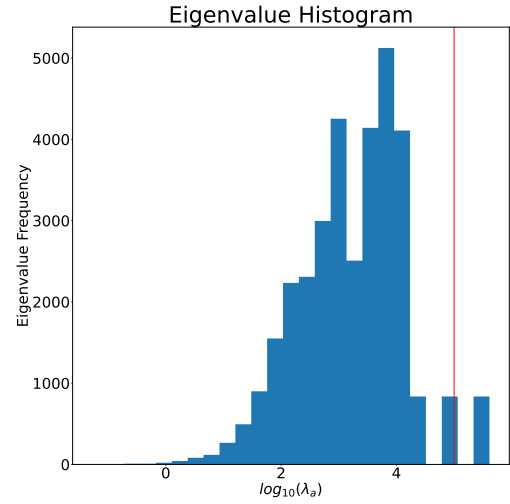
7. Conclusions

We have presented BIPP, an HPC implementation of the Bluebild algorithm. BIPP offers an alternative strategy for interferometric imaging, producing LSQ estimates of the sky using fPCA to reconstruct the sky in distinct energy levels and leveraging the 3D NUFFT to image on the sphere.

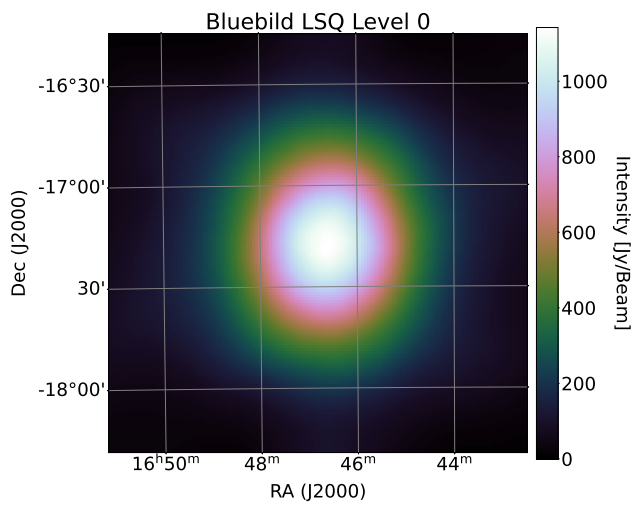
Using BIPP and the new NUFFT Synthesis algorithm we are able to use the Bluebild algorithm with SKA-like array configurations and large image sizes. We show that BIPP reconstructs observations with comparable image fidelity compared to the WSClean w -stacking implementation and improved time-to-solution for image sizes with $N_{\text{pixel}} < 1024^2$. While BIPP does not perform any regularization and the PSF must be removed as a post-processing step, it is a useful option for deconvolution-free imaging.



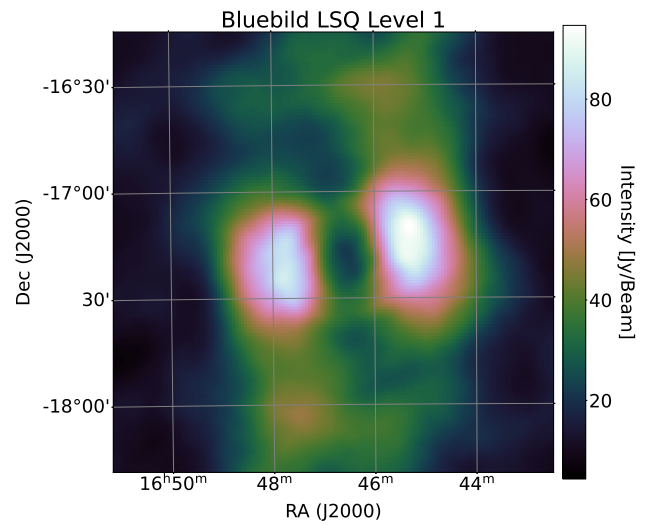
(a)



(b)



(c)



(d)

Figure 9: MWA Observation of the quiet sun decomposed into two eigen-levels by BIPP's functional PCA. (a) shows the least-squares image obtained by summing all least-squared eigen-levels. (b) shows the eigenvalue histogram corresponding to this observation. The red line within the top-right panel shows where the k-means clustering separates least-squared level 0 and least-squared level 1. (c) shows the least-squared level 0 of the MWA solar observation, while (d) shows the least-squared level 1 of the MWA solar observation. Of particular note is the solar limb brightening emission seen in (d), which is not accessible in the dirty images produced by CASA and WSClean.

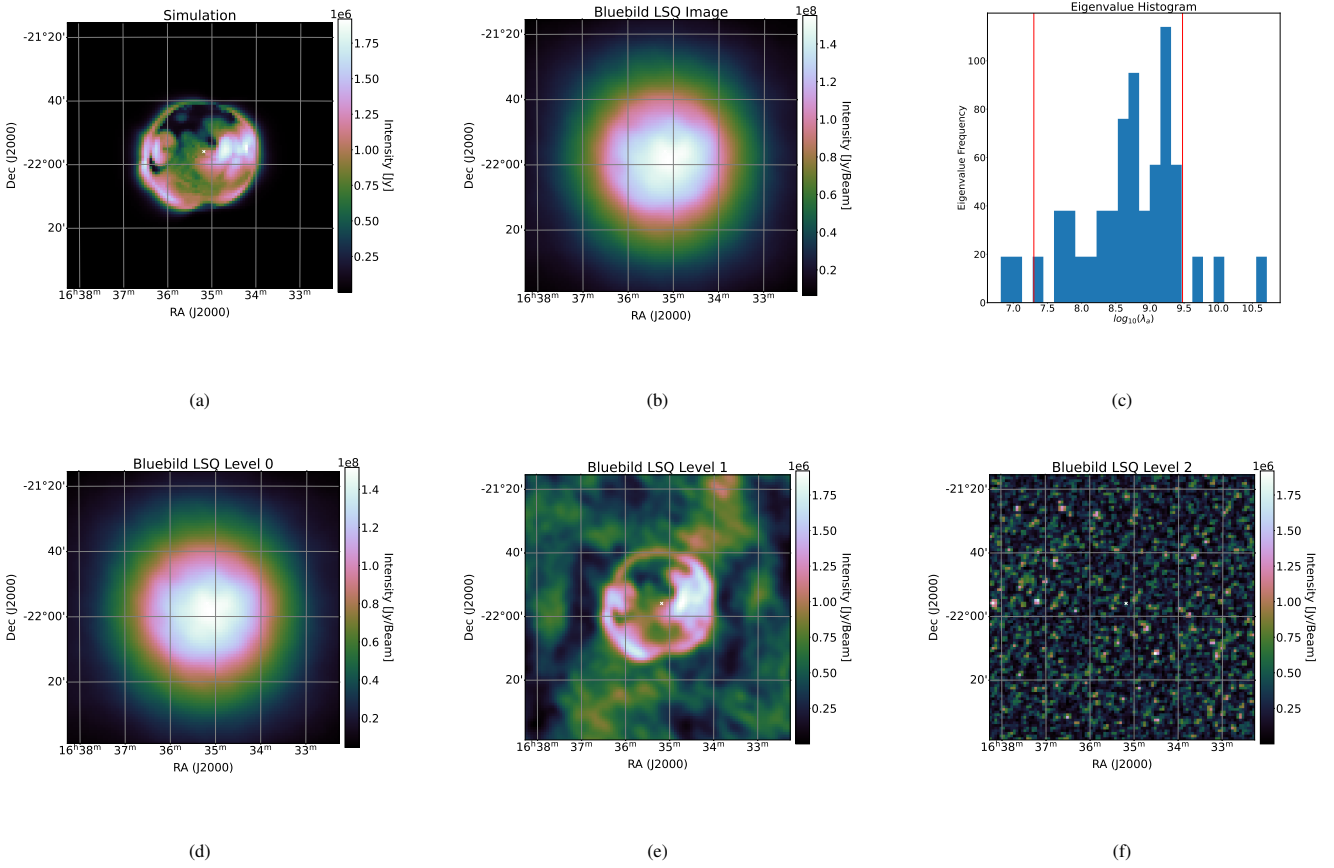


Figure 10: MWA Mock-Observation of FORWARD Solar Simulation. (a) shows the FORWARD simulation that is used as an input sky model to OSKAR. (b) shows the summed BIPP least-squared image. (c) shows the eigenvalue histogram corresponding to this mock-observation, with the red lines showing the separation between different eigen-levels. The bottom row, (d),(e) and (f) shows the least-squares levels 0, 1 and 2. Note the presence of finer features in least-squares level 1, similar to those seen in the FORWARD simulation. Also noteworthy is the absence of these features from (b) which is consistent with the CASA and WSClean dirty images.

We see that for interferometers such as LOFAR, MWA, MeerKAT, and the SKA Mid and Low configurations, the Gram matrix correction has a small effect and the Bluebird LSQ image \tilde{I} is very similar to the dirty image \hat{I} . The Gram matrix correction has a stronger effect if the baseline separation is equal to or smaller than the observing wavelength, which is true for station-level elements of phased array interferometers. However, beamforming is usually performed at the station level and the individual station element data are not available. It is possible to leverage the eigendecomposition offered by Bluebird on the dirty image \hat{I} , which would allow CLEAN algorithms to be run in parallel on the distinct energy levels.

The eigendecomposition provided by BIPP may also allow for scientific analysis that is not possible with combined images. For example, noise suppression can be obtained by discarding the lowest eigenlevels, foreground removal can be achieved by discarding the highest eigenlevels, and interesting substructure may be revealed in intermediate eigenlevels, as shown in Figure 10. Additionally, the decomposition reduces the dynamic range of images, which could be a useful input to AI-based cleaning or analysis techniques.

Future HPC developments of BIPP will focus on scalability, node-level parallelism of the NUFFT, and optimizing our GPU implementation of the type-3 nufft for radio astronomy data. We will also investigate integrating the WStackingGridded⁸ as an alternative image synthesis option.

Acknowledgements

This work was supported by the Platform for Advanced Scientific Computing (PASC) project “Next-Generation Radio Interferometry.” SK acknowledges the financial support from the SNSF under the Sinergia Astrosignals grant (CRSII5_193826). This work has been done in partnership with the SKACH consortium through funding by SERI, and was supported by EPFL through the use of the facilities of its Scientific IT and Application Support Center (SCITAS). The authors gratefully acknowledge the use of facilities of the Swiss National Supercomputing Centre (CSCS). Development of the Bluebird algorithm was supported via the ASTRON-IBM Dome project by the Dutch Ministry of Economic Affairs and by the Province of Drenthe.

We would also like to thank Prof. Oleg Smirnov, Landman Bester, Jonathan Kenyon, and Simon Perkins (SARAO/Rhodes University) for helpful discussions and suggestions regarding interferometry and calibration.

Data Availability

Most of the datasets used in validation are simulated observations generated by open-source libraries as documented in the text. These simulated datasets can be made available upon reasonable request to the authors. The real LOFAR data used for validation are available at DOI:10.5281/zenodo.1042525. The BIPP source code is publically available on GitHub⁹.

References

- Bagchi, S., Mitra, S.K., 1999. *The Nonuniform Discrete Fourier Transform and Its Applications in Signal Processing*. Kluwer Academic Publishers, USA.
- Barnett, A.H., Magland, J., af Klinteberg, L., 2019. A Parallel Nonuniform Fast Fourier Transform Library Based on an “Exponential of Semicircle” Kernel. *SIAM Journal on Scientific Computing* 41, C479–C504. doi:10.1137/18M120885X, arXiv:1808.06736.
- Broekema, P.C., van Nieuwpoort, R.V., Bal, H.E., 2015. The Square Kilometre Array Science Data Processor. Preliminary compute platform design. *Journal of Instrumentation* 10, C07004. doi:10.1088/1748-0221/10/07/C07004.
- Clark, B.G., 1980. An efficient implementation of the algorithm ‘CLEAN’. *A&A* 89, 377.
- Cornwell, T.J., 2008. Multiscale clean deconvolution of radio synthesis images. *IEEE Journal of Selected Topics in Signal Processing* 2, 793–801. URL: <http://dx.doi.org/10.1109/JSTSP.2008.2006388>, doi:10.1109/jstsp.2008.2006388.
- Cornwell, T.J., Golap, K., Bhatnagar, S., 2008. The noncoplanar baselines effect in radio interferometry: The w-projection algorithm. *IEEE Journal of Selected Topics in Signal Processing* 2, 647–657. doi:10.1109/JSTSP.2008.2005290.
- Cornwell, T.J., Perley, R.A., 1992. Radio-interferometric imaging of very large fields. The problem of non-coplanar arrays. *A & A* 261, 353–364.
- Dewdney, P.E., Hall, P.J., Schilizzi, R.T., Lazio, T.J.L.W., 2009. The Square Kilometre Array. *IEEE Proceedings* 97, 1482–1496. doi:10.1109/JPROC.2009.2021005.
- Frigo, M., Johnson, S.G., 1997. *The Fastest Fourier Transform in the West*. Technical Report MIT-LCS-TR-728. Massachusetts Institute of Technology.
- Frigo, M., Johnson, S.G., 2005. The design and implementation of FFTW3. *Proceedings of the IEEE* 93, 216–231. Special issue on “Program Generation, Optimization, and Platform Adaptation”.
- Gibson, S.E., Kucera, T.A., White, S.M., Dove, J.B., Fan, Y., Forland, B.C., Rachmeler, L.A., Downs, C., Reeves, K.K., 2016. Forward: A toolset for multiwavelength coronal magnetometry. *Frontiers in Astronomy and Space Sciences* 3. URL: <https://www.frontiersin.org/articles/10.3389/fspas.2016.00008>, doi:10.3389/fspas.2016.00008.
- Hallinan, G., Ravi, V., Weinreb, S., Kocz, J., Huang, Y., Woody, D.P., Lamb, J., D’Addario, L., Catha, M., Law, C., Kulkarni, S.R., Phinney, E.S., Eastwood, M.W., Bouman, K., McLaughlin, M., Ransom, S., Siemens, X., Cordes, J., Lynch, R., Kaplan, D., Brazier, A., Bhatnagar, S., Myers, S., Walter, F., Gaensler, B., 2019. The DSA-2000 — A Radio Survey Camera, in: *Bulletin of the American Astronomical Society*, p. 255. doi:10.48550/arXiv.1907.07648, arXiv:1907.07648.
- Hamaker, J.P., Bregman, J.D., Sault, R.J., 1996. Understanding radio polarimetry. I. Mathematical foundations. *Astronomy and Astrophysics Supplement* 117, 137–147.
- Högbom, J.A., 1974. Aperture Synthesis with a Non-Regular Distribution of Interferometer Baselines. *Astronomy and Astrophysics Supplement* 15, 417.
- Kashani, S., 2017. Towards real-time high-resolution interferometric imaging with bluebird URL: <http://infoscience.epfl.ch/record/269252>.
- Kashani, S., Rué Queralt, J., Jarret, A., Simeoni, M., 2023. HVOX: Scalable Interferometric Synthesis and Analysis of Spherical Sky Maps. arXiv e-prints , arXiv:2306.06007doi:10.48550/arXiv.2306.06007, arXiv:2306.06007.
- Kemball, A.J., Wieringa, M.H., 2000. Measurement Set definition version 2.0. NRAO report, January 21, 2000, 52 pages.
- Lee, J.Y., Greengard, L., 2005. The type 3 nonuniform fft and its applications. *Journal of Computational Physics* 206, 1–5. URL: <https://www.sciencedirect.com/science/article/pii/S002199910400511X>, doi:https://doi.org/10.1016/j.jcp.2004.12.004.
- McMullin, J.P., Waters, B., Schiebel, D., Young, W., Golap, K., 2007. *CASA Architecture and Applications*, in: Shaw, R.A., Hill, F., Bell, D.J. (Eds.), *Astronomical Data Analysis Software and Systems XVI*, p. 127.
- Mort, B.J., Dulwich, F., Salvini, S., Adami, K.Z., Jones, M.E., 2010. Oskar: Simulating digital beamforming for the ska aperture array, in: *2010 IEEE International Symposium on Phased Array Systems and Technology*, pp. 690–694. doi:10.1109/ARRAY.2010.5613289.
- Offringa, A.R., McKinley, B., Hurley-Walker, et al., 2014. WSClean: an implementation of a fast, generic wide-field imager for radio astronomy. *MNRAS* 444, 606–619. doi:10.1093/mnras/stu1368.

⁸<http://www.andreoffringa.org/wsclean/doxygen/classWStackingGridded.html>

⁹<https://github.com/epfl-radio-astro/bipp>

Offringa, A.R., Smirnov, O., 2017. An optimized algorithm for multiscale wideband deconvolution of radio astronomical images. *MNRAS* 471, 301–316. doi:[10.1093/mnras/stx1547](https://doi.org/10.1093/mnras/stx1547).

Pan, H., Simeoni, M., Hurley, P., Blu, T., Vetterli, M., 2017. Leap: Looking beyond pixels with continuous-space estimation of point sources. *Astronomy & Astrophysics* 608. doi:<https://doi.org/10.1051/0004-6361/201731828>.

Pence, W.D., Chiappetti, L., Page, C.G., Shaw, R.A., Stobie, E., 2010. Definition of the Flexible Image Transport System (FITS), version 3.0. *A & A* 524, A42. doi:[10.1051/0004-6361/201015362](https://doi.org/10.1051/0004-6361/201015362).

Rau, U., Bhatnagar, S., Voronkov, M.A., Cornwell, T.J., 2009. Advances in calibration and imaging techniques in radio interferometry. *Proceedings of the IEEE* 97, 1472–1481. doi:[10.1109/JPROC.2009.2014853](https://doi.org/10.1109/JPROC.2009.2014853).

Schmidt, K., Geyer, F., Fröse, S., Blomenkamp, P.S., Brüggem, M., de Gasperin, F., Elsässer, D., Rhode, W., 2022. Deep learning-based imaging in radio interferometry. *A & A* 664, A134. doi:[10.1051/0004-6361/202142113](https://doi.org/10.1051/0004-6361/202142113), [arXiv:2203.11757](https://arxiv.org/abs/2203.11757).

Sharma, R., Oberoi, D., 2020. Propagation effects in quiet sun observations at meter wavelengths. *The Astrophysical Journal* 903, 126. URL: <https://dx.doi.org/10.3847/1538-4357/abb949>, doi:[10.3847/1538-4357/abb949](https://doi.org/10.3847/1538-4357/abb949).

Shih, Y., Wright, G., Anden, J., Blaschke, J., Barnett, A.H., 2021. cuffnufft: a load-balanced gpu library for general-purpose nonuniform ffts, in: 2021 IEEE International Parallel and Distributed Processing Symposium Workshops (IPDPSW), IEEE Computer Society, Los Alamitos, CA, USA. pp. 688–697. URL: <https://doi.ieeecomputersociety.org/10.1109/IPDPSW52791.2021.00105>, doi:[10.1109/IPDPSW52791.2021.00105](https://doi.org/10.1109/IPDPSW52791.2021.00105).

Simeoni, M., Hurley, P., 2019. Graph spectral clustering of convolution artefacts in radio interferometric images, in: ICASSP 2019 - 2019 IEEE International Conference on Acoustics, Speech and Signal Processing (ICASSP), pp. 4260–4264. doi:[10.1109/ICASSP.2019.8683841](https://doi.org/10.1109/ICASSP.2019.8683841).

Smirnov, O.M., 2011. Revisiting the radio interferometer measurement equation. I. A full-sky Jones formalism. *A & A* 527, A106. doi:[10.1051/0004-6361/201016082](https://doi.org/10.1051/0004-6361/201016082), [arXiv:1101.1764](https://arxiv.org/abs/1101.1764).

Tasse, C., Hugo, B., Mirmont, M., Smirnov, O., Atemkeng, M., Bester, L., Hardcastle, M.J., Lakhoo, R., Perkins, S., Shimwell, T., 2018. Faceting for direction-dependent spectral deconvolution. *A & A* 611, A87. doi:[10.1051/0004-6361/201731474](https://doi.org/10.1051/0004-6361/201731474), [arXiv:1712.02078](https://arxiv.org/abs/1712.02078).

Taylor, G.B., Carilli, C.L., Perley, R.A., 1999. Synthesis imaging in radio astronomy ii, in: *Synthesis Imaging in Radio Astronomy II*.

Taylor, J.M., 1978. The condition of gram matrices and related problems. *Proceedings of the Royal Society of Edinburgh Section A: Mathematics* 80, 45–56. doi:[10.1017/S030821050001012X](https://doi.org/10.1017/S030821050001012X).

The CASA Team, 2022. Casa, the common astronomy software applications for radio astronomy. *Publications of the Astronomical Society of the Pacific* 134, 114501. URL: <https://dx.doi.org/10.1088/1538-3873/ac9642>, doi:[10.1088/1538-3873/ac9642](https://doi.org/10.1088/1538-3873/ac9642).

Thyagarajan, N., Beardsley, A.P., Bowman, J.D., Morales, M.F., 2017. A generic and efficient E-field Parallel Imaging Correlator for next-generation radio telescopes. *Monthly Notices of the Royal Astronomical Society* 467, 715–730. URL: <https://doi.org/10.1093/mnras/stx113>, doi:[10.1093/mnras/stx113](https://doi.org/10.1093/mnras/stx113).

Van der Tol, S., Veenboer, B., Offringa, A.R., 2018. Image domain gridding: a fast method for convolutional resampling of visibilities. *A&A* 616, A27. URL: <https://doi.org/10.1051/0004-6361/201832858>, doi:[10.1051/0004-6361/201832858](https://doi.org/10.1051/0004-6361/201832858).

Tomov, S., Dongarra, J., Baboulin, M., 2010. Towards dense linear algebra for hybrid GPU accelerated manycore systems. *Parallel Computing* 36, 232–240. doi:[10.1016/j.parco.2009.12.005](https://doi.org/10.1016/j.parco.2009.12.005).

van der Veen, A.J., Wijnholds, S.J., 2013. *Signal Processing Tools for Radio Astronomy*. Springer New York, New York, NY. pp. 421–463. URL: https://doi.org/10.1007/978-1-4614-6859-2_14, doi:[10.1007/978-1-4614-6859-2_14](https://doi.org/10.1007/978-1-4614-6859-2_14).

Vetterli, M., Kovačević, J., Goyal, V.K., 2014. *Foundations of Signal Processing*. Cambridge University Press. doi:[10.1017/CB09781139839099](https://doi.org/10.1017/CB09781139839099).

Wilber, A.G., Dabbech, A., Jackson, A., Wiaux, Y., 2023. Scalable precision wide-field imaging in radio interferometry: I. uSARA validated on ASKAP data. *Monthly Notices of the Royal Astronomical Society* 522, 5558–5575. URL: <https://doi.org/10.1093/mnras/stad1351>, doi:[10.1093/mnras/stad1351](https://doi.org/10.1093/mnras/stad1351).

Æçal, O., Hurley, P., Cherubini, G., Kazemi, S., 2015. Collaborative ran-

domized beamforming for phased array radio interferometers, in: 2015 IEEE International Conference on Acoustics, Speech and Signal Processing (ICASSP), pp. 5654–5658. doi:[10.1109/ICASSP.2015.7179054](https://doi.org/10.1109/ICASSP.2015.7179054).

Appendix A. Effect of the Gram Matrix

Recall that the eigenvalue-eigenvector pairs $\{\lambda_a, \alpha_a\}$ are found by solving the generalized eigenvalue problem $V\alpha_a = \lambda_a G\Psi\alpha_a$, therefore:

$$V = G\Psi A \Lambda A^H = G\Psi V', \quad (\text{A.1})$$

where the columns of matrix $A \in \mathbb{C}^{N_A \times N_A}$ are the ordered eigenvectors α_a , Λ is a diagonal matrix with diagonal elements as the ordered eigenvalues λ_a , and V' is what we call the Gram-corrected visibilities.

The least-squares consistent image \tilde{I} constructed by Bluebird is given by:

$$\tilde{I} = \Psi V' \Psi^* \quad (\text{A.2})$$

$$\tilde{I}_j = \sum_n^{N_A \times N_A} V'_n e^{i\langle \vec{b}_n, \vec{r}_j \rangle}, \quad (\text{A.3})$$

and the back-projected image \hat{I} is given by:

$$\hat{I} = \Psi V \Psi^* = \Psi G\Psi V' \Psi^* \quad (\text{A.4})$$

$$\hat{I}_j = \sum_n^{N_A \times N_A} (G\Psi V')_n e^{i\langle \vec{b}_n, \vec{r}_j \rangle}, \quad (\text{A.5})$$

In the context of an NUFFT, the two images have the same input coordinates \vec{b}_n and output coordinates \vec{r}_j , but the sample values differ. We can use the continuous expression of the Gram matrix from Equation 11 to expand our expression for V in terms of V' :

$$V_{pq} = \sum_k^{N_A} (G\Psi)_{pk} V'_{kq} \quad (\text{A.6})$$

$$= \sum_k^{N_A} \text{sinc}\left(2 \left\| \frac{\vec{b}_{pk} f}{c} \right\| \right) V'_{kq} \quad (\text{A.7})$$

$$= V'_{pq} + \sum_{k \neq p}^{N_A} \text{sinc}\left(2 \left\| \frac{\vec{b}_{pk}}{\lambda} \right\| \right) V'_{kq} \quad (\text{A.8})$$

using $\lambda = f/c$. Each visibility V_{pq} can be expressed as a linear combination of the Gram-corrected visibilities V' . The effect of this mixing is larger sidelobes in \hat{I} compared to \tilde{I} .

Note that $\text{sinc}(x) = \sin(\pi x)/\pi x$, so if $\|\vec{b}_{pk}\| \gg \lambda$ for all $k \neq p$ then $V_{pq} \approx V'_{pq}$. This is the case for most modern radio interferometers, so the difference between \hat{I} and \tilde{I} is tiny.

To illustrate the difference between \hat{I} and \tilde{I} , using OSKAR we create simulated SKA-Low telescope observations with a configuration of 512 stations and image a sky model with a single 1000 Jy source. We image at 53MHz and 89MHz as the off-diagonal terms of the Gram matrix become larger at lower frequencies as shown in Eq. 11. When imaging at 53MHz we

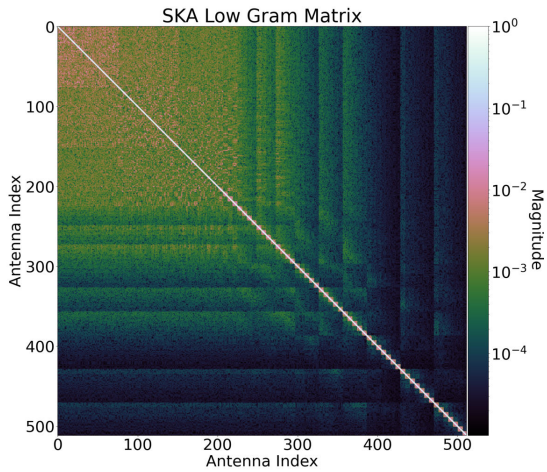


Figure A.11: The Gram matrix visualised for the simulated SKA-Low array at 53 MHz.

use a FoV of 1.16692 degrees and when imaging at 89MHz we use a FoV is 0.7002 degrees. This sky model is observed over 1 epoch. The resulting Gram matrix for 53MHz can be seen in Figure A.11, and contains nonzero off-diagonal terms.

The visibilities obtained from these simulated observations are then imaged using BIPP with and without using the Gram matrix and shown Figures A.12 and A.13. The presence of negative artefacts from the interferometric sidelobes in the residual image tells us that the sidelobes are more intense when using BIPP without the Gram matrix compared to using BIPP with the Gram matrix. Furthermore, we see in Figure A.13 that this effect is more pronounced at lower frequencies. This can be observed in the magnitude of the residuals, which are stronger for the 53 MHz case compared to the 89 MHz case.

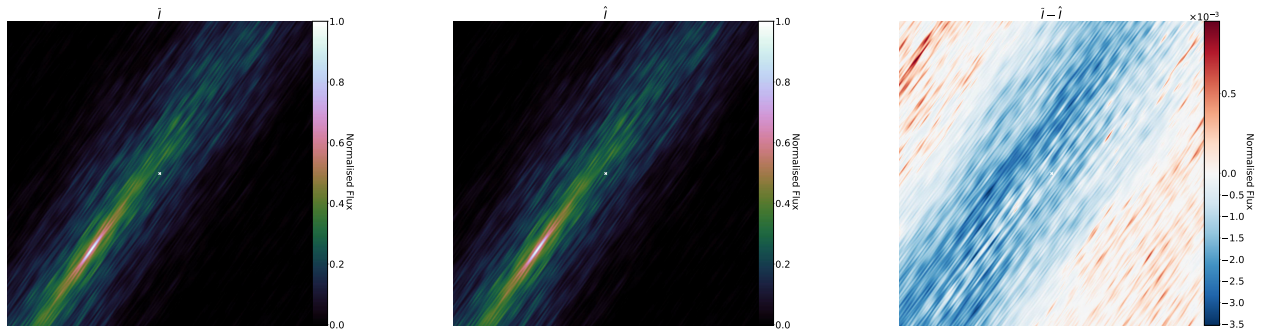


Figure A.12: The effect of using the Gram matrix for the generalized eigenvalue decomposition in BIPP reconstructed images at 53MHz. The left column subplot contains the BIPP image normalised by its maximum value. The middle subplot contains the reconstructed BIPP image with the Gram matrix set to identity. This has also been normalised by its maximum value. The right subplot shows the residual obtained when taking the difference between the BIPP images reconstructed with and without the Gram matrix. The presence of negative (blue) features in the residual image tells us that the sidelobes are slightly stronger when the Gram matrix is turned off.

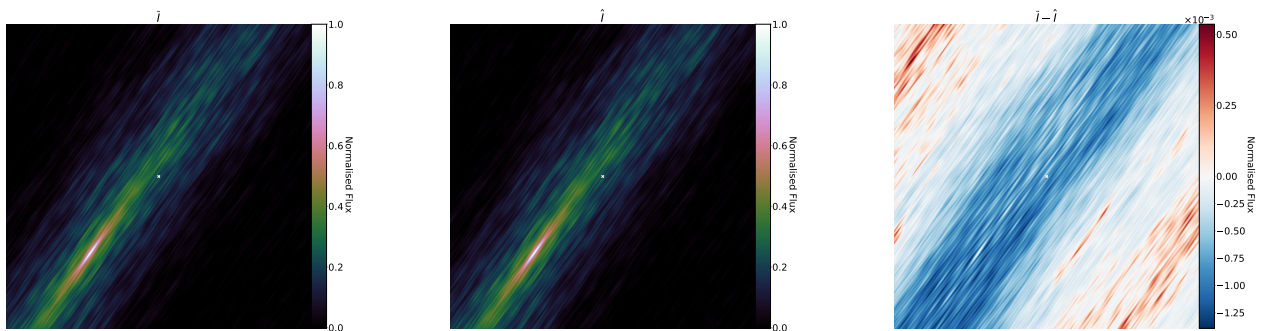


Figure A.13: The effect of using the Gram matrix for the generalized eigenvalue decomposition in BIPP reconstructed images at 89MHz. The left column subplot contains the BIPP image normalised by its maximum value. The middle subplot contains the reconstructed BIPP image with the Gram matrix set to identity. This has also been normalised by its maximum value. The right subplot shows the residual obtained when taking the difference between the BIPP images reconstructed with and without the Gram matrix. The presence of negative (blue) features in the residual image tells us that the sidelobes are slightly stronger when the Gram matrix is turned off.